The contribution of the bolting system to the shear stiffness of circumferential joints in tunnel segmental linings

Computers and Geotechnics 162 (2023) 105660

Contents lists available at ScienceDirect

Computers and Geotechnics

journal homepage: www.elsevier.com/locate/compgeo

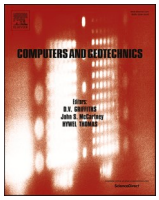

The contribution of the bolting system to the shear stiffness of circumferential joints in tunnel segmental linings

Xin Han [a,b], Pierpaolo Oreste [b,*], Fei Ye [a]

[a] School of Highway, Chang'an University, Middle-section of Nan'er Huan Road, Xi'an 710064, Shaanxi Province, China
[b] Department of Environment, Land and Infrastructure Engineering (DIATI), Politecnico di Torino, Corso Duca degli Abruzzi 24, 10129 Torino, Italy

ARTICLE INFO

Keywords:
Tunnel segmental lining
Circumferential joints
Bolting system
Shear stiffness
Finite Element Method
Numerical modelling

ABSTRACT

The tunnel segmental lining is a type of support structure that is very complex and widely used in tunnel excavation. Of particular importance is the behaviour of circular joints in contact with adjacent rings.

The shear behaviour of the circular joint is studied in detail in this paper. Particularly, bolts, which are widely used to connect the adjacent segments, play a fundamental role in the mechanical behaviour of the circular joints and therefore of the tunnel segmental lining.

A new FEM model has been developed to be able to analyse the shear deformation of bolts, when two adjacent segments show a relative transversal displacement. The model allows to consider also the interaction of the bolt with the walls of the hole. It was possible to obtain the trend of the shear stiffness of the circular joint as the relative transversal displacements varied.

A successfully comparison of the calculation results with the laboratory measurements was obtained. Some suggestions are proposed in order to enhancing the practicality of the model. The proposed numerical model is a useful calculation tool capable of correctly evaluating the mechanical behaviour of the circular joints and therefore to correctly represent them during the design stage.

1. Introduction

Adopting TBM to construct the tunnel, the ground is supported by the precast concrete segments connected by bolts. Therefore the tunnel lining is composed of segments and joints (including transverse joints and longitudinal joints); furthermore, the joints consist of bolts and the concrete body (joint influenced zone) which is the edge part of the segments having bolt holes inside (Fig. 1) (Do et al., 2015; Zaheri et al., 2020).

Due to the weaker stiffness of joints than the one of the segmental lining, the deformation magnitude of the joints is larger than the one of segments along the longitudinal direction, and the relative movement of the adjacent rings caused by external loads leads to a decrease of the stressed zone size and to an increase of the stress values, which results in a stress concentration and eventually a lining damage. Liu et al. (2020b) reported that the leakage inside a lining leads to the settlement of the segmental lining, which causes a relative dislocation of adjacent rings and also a sever spalling along the circumferential joint. Huang et al. (2020) described an incident of Tianjin metro (China), where the sand and water flow into the tunnel along the 42 mm drilling hole of the steel segments used for a crossing passage, led to cracks and spallation along the circumferential joint. In these two cases, joints are the vulnerable zone compared with segments when the large deformations of the segmental lining happen, and an induced high stress concentration along the joint can be dangerous. More specifically, the load on the segmental lining during the tunnel construction is generally unevenly distributed, and also the movements of the lining along the longitudinal direction and the transversal direction are presented in that period (Chen et al., 2018; Feng et al., 2022; Gil Lorenzo, 2019; Han et al., 2023a; Oreste et al., 2021; Zhou and Ji, 2014). Therefore, it is important in the design stage to develop an evaluation of the induced transient stress concentration in the segmental lining, using specific methods considering the changeable contact among segments and the bolt presence along the circumferential joints.

When evaluating the segment behaviours, the analytical method based on some parameters is widely used beside the experimental method and the empirical one. The analytical method includes the analytical computing, 3D and 2D numerical modelling. A numerical model can be able to calculate the stress and strain distribution along the longitudinal and circumferential direction of a segmental lining (Chaipanna and Jongpradist, 2019; Dastjerdy et al., 2018; Do et al., 2016; Do et al., 2013; Wang et al., 2021). When a lining is analysed, a new model

* Corresponding author.

https://doi.org/10.1016/j.compgeo.2023.105660
Received 27 February 2023; Received in revised form 19 June 2023; Accepted 10 July 2023
Available online 31 July 2023

has to be built, and the time-consuming of the model building and of the calculation of the results restricts its widespread use.

With reference to the analytical computing, the beam theory is usually adopted to evaluate the deformations of a segmental lining along the longitudinal direction (Huang et al., 2015; Huang et al., 2022; Liang et al., 2020; Liang, 2019; Liang et al., 2017; Shi et al., 2022; Wu et al., 2015; Wu et al., 2018). Based on the simplification of the joint behaviour, these theories can be divided into two categories: beam-spring model (Koizumi et al., 1988) and continuous beam model (Shiba et al., 1988). In the beam-spring model, the segmental rings are simplified as a short beam and the joints are represented by the axial, shear and rotational springs. Because it is difficult to determine the stiffness of the springs, the beam-spring model is used limitedly. For the continuous beam model, the Euler-Bernoulli beam and the Timoshenko beam are adopted to analyse the longitudinal deformation of the segmental lining. In order to obtain the analytical solution, the continuous beam model simply consider the lining ring and the joint as an equivalent continuous beam, and it is difficult to display the difference between the lining ring deformation and the joint deformation. However, when the dislocation and the damage of a segmental joint have to be analysed, the behaviour of the circular joint is important. Combining the advantages of the numerical model and the beam theory, the numerical beam-spring method is used to evaluate the lining ring deformation (Do et al., 2014; Oreste, 2007; Oreste et al., 2018) and the lining deformation along the longitudinal direction (Han et al., 2023a). On these analytical models, the stiffness of the joint is the key parameter: it includes both the bending stiffness and the shear stiffness.

For the bending stiffness, the relative rotation between the adjacent surfaces of joints will determine the contact area and the stress transmission between the segments. Shiba et al. (1988) analysed the deformation and the stress along the joint when the normal force is equal to zero, and developed the bending stiffness equation considering the joint opening rotation. Some authors (Cheng et al., 2021; Huang et al., 2015; Liao et al., 2008; Wu et al., 2015; Yu et al., 2019) developed models by considering the influencing length of the joints. Li et al. (2019) carried out an indoor experiment to test the bending stiffness with different normal (longitudinal) force acting on the circular joint, and obtained a bending stiffness equation which depends on the normal force and the moment. Geng et al. (2019) and Wang et al. (2022) divided the deformation of the joint into different patterns based on the joint opening magnitude, and obtained an equivalent bending stiffness under the application of the normal force. Based on the finite element theory, Han et al. (2023b) developed a bending stiffness equation for the joint element on the basis of the transformed area method, which can be used to calculate the bending stiffness and the deformation state of a joint (from the joint closed to the open case) under a normal force.

Compared with the bending deformation, the shear deformation is more complex and insufficient attention paid to it in the scientific literature. Based on the test results, the dislocation of a joint under the shear force can be divided into three phases: static friction phase, bolt (and concave and convex tenon) sheared phase, damage phase (Cheng et al., 2021; Liu et al., 2018; Zuo et al., 2022). Due to the scarcity of available trials and specimens, the numerical modelling of a circular joint was applied to analyse the joint shear deformation behaviour (Li et al., 2014; Wang et al., 2021). Furthermore, an equivalent shear stiffness equation was developed with the segmental lining deformation along the longitudinal direction. When the Euler–Bernoulli beam theory is used to analyse the segmental lining deformation, the shear deformation is ignored (Talmon and Bezuijen, 2013). Afterward, using the Timoshenko beam theory for the analysis of the segmental lining deformation, the equation of the equivalent share stiffness is developed simultaneously (Cheng et al., 2021; Liang et al., 2017; Liu et al., 2021a; Wang et al., 2022; Wu et al., 2015). Based on the results of Wu et al. (2015) and Liang et al. (2017), reducing the shear stiffness of the joint leads to an increase of the dislocation and a decrease of the joint opening and of the segment rotation. Therefore, an accurate evaluation of the joint shear stiffness is very important for the analysis of the segmental lining behaviour. Some aspects must be considered in the three main phases of the shear dislocation of a circular joint: firstly, the friction is influenced by the surface smoothness of the segments and by the normal force; secondly, the shear deformation of the bolting system depends on the bending stiffness of each bolt, the concrete foundation modulus and the strength of steel and concrete; thirdly, the shear deformation of the tenon has a significant relationship with the tenon sizes and its strength.

In this paper, focusing on the bolt deformation during relative displacements of segments, the shear stiffness of the circular joint is investigated. Based on the beam-spring method, a new FEM model was developed to evaluate the shear deformation of the straight bolt and the influence of the concrete foundation modulus. Furthermore, using the same FEM model the curved bolt was also studied with its influence on the shear stiffness of the joint. Regarding the shear deformation of each bolt, four different combinations of the constraints on the bolt endpoint

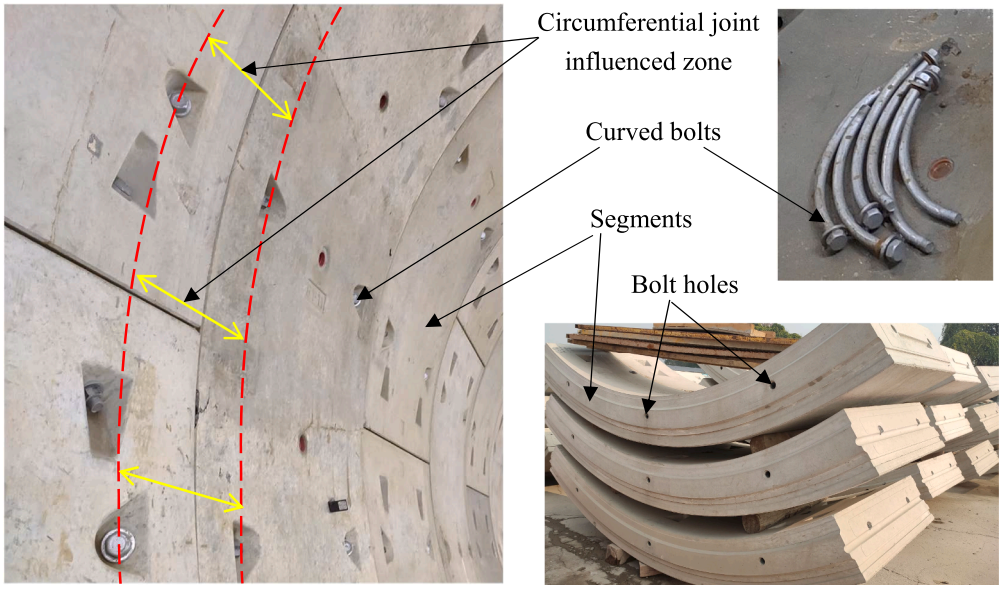

Fig. 1. The components of segmental lining joints.

were considered and discussed. The influences of the bolt pretension and of the gap between the bolt and the hole wall on the maximum shear force and the tensile force in the bolt were analysed, and the stresses on the material are compared with the yielding strength of the steel and concrete. Finally, the calculation results obtained by the proposed model were compared successfully with available laboratory test results in the scientific literature. Some suggestions are finally proposed for the segmental lining design based on the considerations that emerged from the study.

The proposed calculation model can therefore be very useful in the design phase of sizing the segmental lining, allowing the circular joint to be represented in the numerical simulations with an appropriate shear stiffness. This stiffness, in fact, constitutes a fundamental parameter to be able to study in detail the behavior of the segmental lining and to evaluate stresses and deformations that develop inside it.

2. Shear stiffness evaluation and equations available in the scientific literature

2.1. Short review of researches about the shear deformation and the damage of circular joints

Based on the forms of joint, the circular joint can be divided into flat joint and tenon joint. The flat joint is composed of the bolt and the shear force is undertaken by the bolt (Fig. 2a). The tenon joint is composed of the bolt and the tenon (including the concave tenon and convex tenon, Fig. 2b, 2c, 2d). The tenon joint can be further divided into the distributed tenon joint (Fig. 2b & 2c) and the continuous tenon joint (Fig. 2d) based on the distribution of the tenon along the circumferential joint.

For the tenon joint, the main factors which influence the shear deformation of the joint include three parts: the friction force between segments, the shear deformation of the tenon, the shear deformation of the bolt. The friction force between the segments depend on the normal force and the friction angle of the joint, and is the main reason to restrict the relative movement of segments on the joint before the contact of the tenons and the bolts with the hole walls due to the gaps between the concave tenon and the convex one and between the bolt and the hole wall (Liu et al., 2018; Zuo et al., 2022). When the shear force on the joint is larger than the static friction force, the tenon and the bolt will resist the relative displacement and undertake the shear force. Compared with the indoor test, the numerical model can show the stress of the tenon and the bolt separately. Zhang et al. (2020) and Zhao et al. (2022) analysed the stress state of the continuous tenon and the distributed one using a numerical model. The maximum shear force of the tenon and the corresponding relative displacement are shown in Table 1. From Table 1 it is possible to note how the continuous tenon reaches the maximum shear force with a small relative displacement which is about 0.1–0.3 mm, while the distributed one reaches the limit stress state when the relative displacement is about 1 mm. Furthermore, the damage location of the continuous tenon results to be always the concave tenon, which may produce the breakage of the concrete. The distributed tenon shows more ductility than the continuous one. After reaching the limit stress state, the shear force of the tenon decreases, and the opening and rotation of the joint is observed from the indoor tests (Liu et al., 2021b; Zuo et al., 2022); it means that the residual shear force of the tenon will continue to influence the shear deformation of the joint, and the shear force undertaken by the tenon will be released and transferred to adjacent bolts. Although the shear force on the joint is undertaken by the bolts and the tenons after the friction phase, the behaviour and contribution of bolts and tenons are not clear.

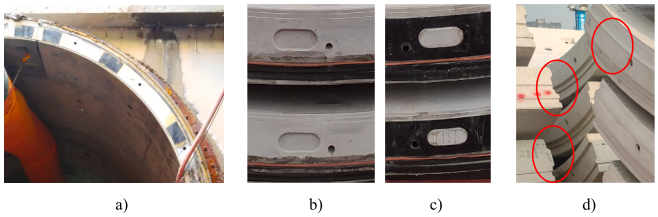

a) b) c) d)

Fig. 2. The component of the segmental lining joint. Key: a) Flat joint; b) The concave tenon of the distributed tenon joint; c) The convex tenon of the distributed tenon joint; d) Continuous tenon joint.

Table 1
The relative displacement of the concave and convex tenons and the reached maximum shear force in numerical model on segment joints (data obtained from published results).

Maximum shear force (kN)	Corresponding displacement (mm)	Damage location	Type of the tenon joint	Reference from
322.93	0.21	concave tenon	Continuous tenon	Zhang et al. (2020)
193.17	0.27	concave tenon	Continuous tenon	Zhang et al. (2020)
147.58	0.11	concave tenon	Continuous tenon	Zhao et al. (2022)
361.79	0.95	concave tenon & convex tenon	Distributed tenon	Zhao et al. (2022)
364.36	1.02	concave tenon & convex tenon	Distributed tenon	Zhao et al. (2022)
128.47	0.96	concave tenon & convex tenon	Distributed tenon	Zhao et al. (2022)

2.2. Short review of solutions for equivalent shear stiffness in the scientific literature

In order to analyse the tunnel shear deformation along the longitudinal direction, Wu et al. (2015) developed an equivalent shear stiffness equation (Eq. (1)) based on the displacement of the segmental lining along the joint under the application of a shear force.

$$(k \bullet G \bullet A_J)_{eq} = \xi \frac{l_s}{\left(\frac{l_b}{m \bullet k_b \bullet G_b \bullet A_b} + \frac{l_s - l_b}{k_s \bullet G_s \bullet A_s}\right)} \tag{1}$$

where $(k \bullet G \bullet A_J)_{eq}$ is the equivalent shear stiffness of joint, l_s is the length of the segmental lining ring, l_b is the length of longitudinal bolts; m is the total number of bolts on the joint; k_b is the shear coefficient of the bolt based on the Timoshenko beam assumption, and it is equal to 0.9 for a circular section, k_s is the one of the segmental lining ring, and is equal to 0.5 for the annular cross section; G_b is the shear modulus of the bolt, G_s is the one of the ring; A_b is the transverse area of the bolt, A_s is the one of the ring; ξ is a modifying factor.

The Eq. (1) is widely used to calculate the tunnel shear deformation based on the Timoshenko beam theory (Liang et al., 2017; Liu et al., 2020a; Liu et al., 2021a; Shi et al., 2022; Yu et al., 2022).

On the basis of experimental results, Cheng et al. (2021) divided the shear deformation of a joint into three stages: a static friction stage (I), a gap close stage (II) and a bolt (or tenon) shear deformation stage (III). Considering the influence of the rubber gaskets on the joint, the stiffness of the stage I is neglected, and Cheng et al. (2021) derived the shear stiffness for the stage II (Eq. (2)) and stage III (Eq. (3) for the bolt shear deformation alone and Eq. (4) considering also the tongue and groove tenon shear deformation).

$$(k \bullet G \bullet A_J)_{eq,II} = \frac{l_s}{\left(\frac{\lambda \bullet l_b}{(k \bullet G \bullet A_J)_g} + \frac{l_s - \lambda \bullet l_b}{k_s \bullet G_s \bullet A_s}\right)} \tag{2}$$

$$(k \bullet G \bullet A_J)_{eq,III,bolt} = \frac{l_s}{\left(\frac{\lambda \bullet l_b}{m \bullet k_b \bullet G_b \bullet A_b} + \frac{l_s - \lambda \bullet l_b}{k_s \bullet G_s \bullet A_s}\right)} \tag{3}$$

$$(k \bullet G \bullet A_J)_{eq,III,boltandtenon} = \frac{l_s}{\left(\frac{\lambda \bullet l_b}{m \bullet k_b \bullet G_b \bullet A_b + k_g \bullet G_g \bullet A_g} + \frac{l_s - \lambda \bullet l_b}{k_s \bullet G_s \bullet A_s}\right)} \tag{4}$$

where $(k \bullet G \bullet A_J)_{eq,II}$ is the equivalent shear stiffness of joint for the stage II, $(k \bullet G \bullet A_J)_{eq,III}$ is the equivalent shear stiffness of joint for the stage III; λ represents the influenced length factor of the joint for the segmental lining; $(k \bullet G \bullet A_J)_g$ is the shear stiffness of the joint during the gaps closing on the stage II; k_g, G_g and A_g are the Timoshenko shear coefficient, the shear modulus and the shear area of the groove, respectively.

The equations of Wu et al. (2015) and Cheng et al. (2021) are based on the assumption that the shear force is undertaken by the bolt, and are derived by considering that the shear stiffness of the joint is equal to the one of the bolt. These simple equations clearly describe the weaker shear stiffness of the joint. However, due to the existing of the gap between the bolt and hole wall, there is a shear deformation phase that the bolt can move without restricted force from the hole wall; additionally, because the stiffness of the concrete is smaller than the one of steel, which can be found based on the elastic modulus of the bolt and the concrete ($E_{bolt} \gg E_{concrete}$), the concrete has a more significant deformation when the bolts and the concrete hole wall squeeze each other. In short, there is a greater shear deformation of the joint when considering the gap and the concrete compression deformation, and for this reason the shear stiffness of the circular joint between the segmental rings is generally overestimated, which is confirmed on Sect. 3.2.

By analysing the deformation of the bolt in the hole, Han et al. (2023b) developed a calculation procedure for the equivalent shear stiffness evaluation considering the bolt as a cantilever beam (Fig. 3). However, due to the real shape of the bolt, the geometry of the bolt hole and the construction loads that are different among the tunnel projects, this model is not able to express the bolt shear deformation in all the real cases.

2.3. Short review of researches about bolt action in the scientific literature

The joint deformation due to the bolt action requires the analysis of the interaction between the bolt and the bolt hole. Many researches focused on the bolt deformation in rock joints and the steel deformation in the concrete, and analysed the dowel action of the bolt on the joint (Ma et al., 2018; Moradi et al., 2012; Oreste, 2009; Oreste and Cravero, 2008; Ranjbarnia et al., 2014; Sørensen et al., 2017).

The dowel action of the bolt is classically described based on the theory of a beam on elastic foundation (BEF model) (Fig. 4). Based on the results of the Ma et al. (2018), the shear deformation of the bolt depends on the mechanical properties of the concrete and the bolt (Eq. (5) and Eq. (6)).

$$Q_0 = \frac{k}{2 \bullet t} \bullet v_0 \tag{5}$$

$$t = \sqrt[4]{\frac{k}{4E \bullet I}} \tag{6}$$

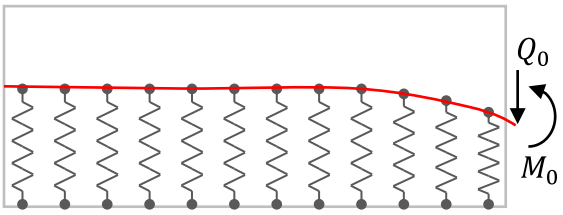

Fig. 4. A calculation model of the bolt action considering the elastic foundation (Winkler approach) to simulate the interaction with the bolt hole (after Ma et al., 2018).

where Q_0 is the external shear load on the bolt at the point of the joint, v_0 is the displacement of the bolt at that point; k is the spring stiffness of concrete which is able to describe the reaction force of the concrete on the bolt, which is equal to the concrete foundation modulus k_c multiply the bolt diameter $k = k_c \bullet d_b$, E is the elastic modulus of the bolt material (steel), I is the inertia moment of the bolt cross-section depending on the bolt diameter, $I = \pi \bullet d_b^4/64$, d_b is the diameter of the bolt.

Considering the influence of the concrete, three critical aspects need to be analysed: the concrete foundation modulus, the ultimate load capacity of the concrete, and the bolt yielding and failure criteria.

For the concrete foundation modulus, Soroushian et al. (1987) based on laboratory experiments suggested to adopt the following equation:

$$k_c = \frac{127 \bullet f_{cc}^{0.5}}{(d_b)^{\frac{2}{3}}} \tag{7}$$

where f_{cc} is the compressive strength of concrete (MPa), the unit of d_b is mm.

Maekawa and Qureshi (1996) obtained a similar equation for concrete, which is modified by Moradi et al. (2012):

$$k_c = \frac{150 \bullet f_{cc}^{0.85}}{d_b} \tag{8}$$

Vintzēleou and Tassios (1986) studied the damage model of concrete under the dowel action of the bolt; two different models were considered: Model A) bolt yielding and concrete crushing; Model B) concrete splitting. Based on test results, the damage model depends on the thickness of the concrete which is compressed by the bolt (when the concrete thickness is larger than 6–7 times the bolt diameter, the failure model is the Model A; otherwise, the failure model is the Model B). Regarding the Model A, Vintzēleou and Tassios (1986) obtained the maximum compressive stress in the concrete by applying a concentrated load on an infinite cohesive material. Regarding the Model B, Soroushian et al. (1986) tested the bearing strength of the concrete when the concrete begins to crack.

Under the contemporary application of the axial force (N_L), the bending moment (M_L) and the shear force (V_L), the criteria of the determination of the bolt condition include two main methods. The main difference between them is the combination among the ratios of the axial force, bending moment and the shear force with the corresponding ultimate values, respectively, (N_L/N_f), (M_L/M_f), (V_L/V_f), where N_f is the ultimate axial force, $N_f = f_y \bullet A_b$, M_f is the ultimate moment, $M_f = f_y \bullet d_b^3/6$, V_f is the ultimate shear force, $V_f = f_y \bullet A_b/\sqrt{3}$

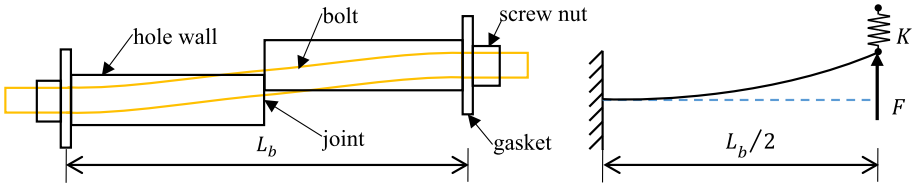

Fig. 3. The model of shear deformation of the bolt in the bolt hole and the mechanical model assumed by (after Han et al., 2023b).

(based on Von-Mises criteria), f_y is the ultimate axial stress of bolt. (Ma et al., 2019; Maekawa and Qureshi, 1996).

The first type of the failure criteria considered the combination of the axial force and the shear force:

$$\left(\frac{V_L}{V_f}\right)^2 + \left(\frac{N_L}{N_f}\right)^2 = 1 \tag{9}$$

The second one is obtained on the basis of the bending moment together with the axial force:

$$\frac{M_L}{M_f} + \left(\frac{N_L}{N_f}\right)^2 = 1 \tag{10}$$

Based on the Von-Mises criteria, the failure criteria is defined considering the bending moment, the shear force and the axial force (Maekawa and Qureshi, 1996) in the following way:

$$\left[\frac{M_L}{M_f} + \left(\frac{N_L}{N_f}\right)^2\right]^2 + \left(\frac{V_L}{V_f}\right)^2 = 1 \tag{11}$$

However, there is a great difference between the bolt inserted in the segmental lining joint and the case of an embedded bolt, such as the bolt inside a rock mass or the bolt inside the concrete. For the convenience to install the bolt in the segmental lining joint, a gap between the bolt and bolt hole has to be foreseen, and the wrapping force in the bolt can be neglected. Furthermore, the shape of the bolt and the load condition are not uniform, such as for a straight bolt, a curved bolt, and a inclined bolt (Fig. 5).

3. Analysis in the detail of the bolt deformation under a relative transversal movement between lining rings and the effects of the bolt-concrete contact

Considering the bolt shape, the simplest case of a straight bolt is firstly analysed to evaluate the main influencing factors on the mechanical behaviour of the bolt in the circular joint.

3.1. Shear deformation model of the straight bolt

The locations of the straight bolt and the bolt hole before and after the lining dislocation are shown in Fig. 6a, where the potential compressive zones on the hole wall (contact zone) are marked by a red line. Due to the existence of the gap between the bolt and bolt hole, the compressive zone is not present along the whole bolt. For the interaction between the bolt and the bolt hole, Winkler springs are used to represent the reaction force of the compressed hole wall, and the spring works only when the bolt transversal displacement is larger than half of the gap (Fig. 6b), defined as the difference between the hole diameter and the bolt diameter.

Using the Finite Element Method (FEM), the bolt can be regarded as a combination of beam elements. Due to the symmetry of the problem with respect of the joint, only one half of the bolt is simulated in the model.

Based on the Timoshenko beam theory and the FEM, the stiffness matrix of bolt element $[k_b]_i$ can be obtained:

$$[k_b]_i = \frac{E \bullet I}{l^3}\begin{bmatrix} \frac{12}{1+\Phi} & \frac{6l}{1+\Phi} & -\frac{12}{1+\Phi} & \frac{6l}{1+\Phi} \\ \frac{6l}{1+\Phi} & \frac{4+\Phi}{1+\Phi}l^2 & -\frac{6l}{1+\Phi} & \frac{2-\Phi}{1+\Phi}l^2 \\ -\frac{12}{1+\Phi} & -\frac{6l}{1+\Phi} & \frac{12}{1+\Phi} & -\frac{6l}{1+\Phi} \\ \frac{6l}{1+\Phi} & \frac{2-\Phi}{1+\Phi}l^2 & -\frac{6l}{1+\Phi} & \frac{4+\Phi}{1+\Phi}l^2 \end{bmatrix} \tag{12}$$

where l is the length of the bolt element, Φ is the ratio between the bending stiffness and the shear stiffness of the bolt, and can be calculated by the following equation:

$$\Phi = \frac{12 \bullet (E \bullet I)}{(k_b \bullet G_b \bullet A_b) \bullet l^2} \tag{13}$$

The sub matrix $[k_{i,a}]$ of the matrix $[k_b]_i$ is used to express the first four element of matrix,

$$[k_{i,a}] = \frac{E \bullet I}{l^3}\begin{bmatrix} \frac{12}{1+\Phi} & \frac{6l}{1+\Phi} \\ \frac{6l}{1+\Phi} & \frac{4+\Phi}{1+\Phi}l^2 \end{bmatrix} \tag{14}$$

Together with the sub matrix $[k_{i,b}]$, $[k_{i,c}]$, $[k_{i,d}]$, the matrix $[k_b]_i$ can be written as follows:

$$[k_b]_i = \begin{bmatrix} k_{i,a} & k_{i,b} \\ k_{i,c} & k_{i,d} \end{bmatrix} \tag{15}$$

Therefore, the global matrix of the bolt $[K]$ can be obtained based on the local matrixes of each element, assembling them along the diagonal:

$$[K] = \begin{bmatrix} k_{1,a} & k_{1,b} & 0 & \cdots & 0 & 0 \\ k_{1,c} & k_{1,d}+k_{2,a} & k_{2,b} & \cdots & 0 & 0 \\ 0 & k_{2,c} & k_{2,d}+k_{3,a} & \cdots & 0 & 0 \\ \vdots & \vdots & \vdots & \ddots & \vdots & \vdots \\ 0 & 0 & 0 & \cdots & k_{n-1,d}+k_{n,a} & k_{n,b} \\ 0 & 0 & 0 & \cdots & k_{n,c} & k_{n,d} \end{bmatrix} \tag{16}$$

Furthermore, the external nodal forces vector can be represented by the nodal displacements vector and the global matrix:

$$[F] = [K] \bullet [S] \tag{17}$$

where

$[F]$ is the vector of the nodal forces, $[F] = [F_1 \quad F_2 \quad F_3 \quad F_4 \quad \cdots \quad F_n \quad F_{n+1}]^T$; F_i $(i = 1, 2, 3, \cdots, n+1)$ are the external forces on nodes which include the transversal force V_i and the bending moment R_i of node i, $F_i = [V_i \quad R_i]^T$.

$[S]$ is the vector of the nodal displacements, $[S] = [S_1 \quad S_2 \quad S_3 \quad S_4 \quad \cdots \quad S_n \quad S_{n+1}]^T$; S_i $(i = 1, 2, 3, \cdots, n+1)$ consists of the transversal displacement v_i and the rotation angle θ_i of node i, $S_i = [v_i \quad \theta_i]^T$.

When considering the interaction between the bolt and the concrete hole, an adding term $[K_c]_{i,a}$ is supplemented in the global stiffness matrix $[K]$ along the diagonal due to the reaction force of the hole wall produced by the bolt transversal displacement, (Oreste, 2007):

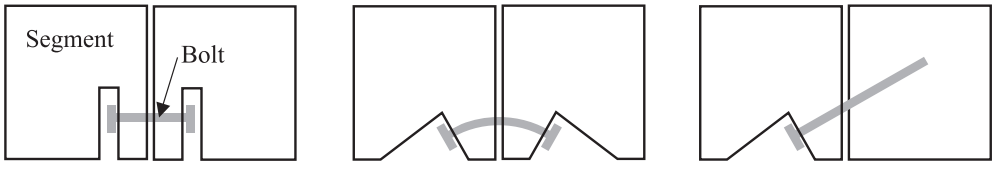

Fig. 5. The connection types with bolts between segments in a circular joint of the tunnel segmental lining. Key: a) Straight bolt; b) Curved bolt; c) Inclined bolt.

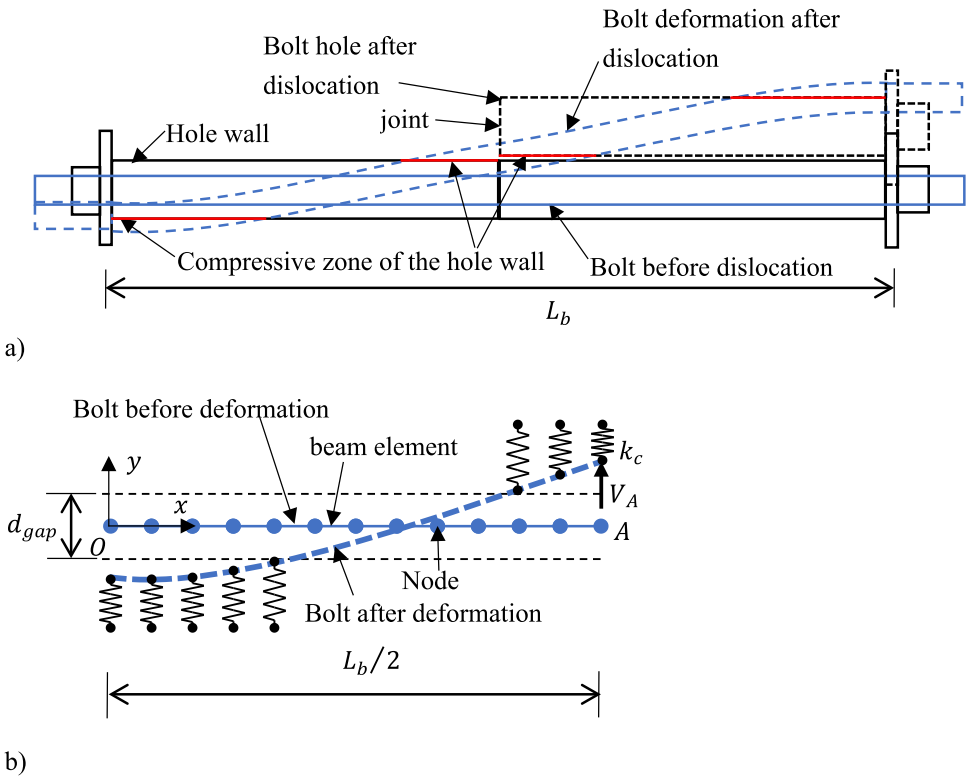

Fig. 6. The bolt deformation under the application of a shear force on the circular joint. Key: a) bolt deformation in the hole; b) assumed mechanical model of the bolt deformation and the interaction bolt-hole.

$$[K_c]_{i,a} = \begin{bmatrix} k_c \bullet l_{av,i} \bullet d_b & 0 \\ 0 & 0 \end{bmatrix} \tag{18}$$

where $l_{av,i}$ is the average length of the elements bordering the node i; k_c is influenced by the compressive strength of concrete and the diameter of the bolt based on Eq. (7) and Eq. (8) (He and Kwan, 2001; Matsunaga et al., 2021; Moradi et al., 2012; Sørensen et al., 2017); Eq. (7) is adopted in this paper, and the influence of concrete foundation modulus on the shear stiffness of joint is discussed on the next section. Whether the reaction springs work depends on the transversal displacement of the nodes in the bolt on the cross section of bolt hole. When the nodes in the bolt reach to the hole wall, an additional force $F_{i,a}$ should be added to F_i correspondingly, because an extra reaction force is added to the right side ($[K] \bullet [S]$) of Eq. (17) based on Eqs. (16) and (18), which is equal to the spring stiffness multiply by half of the gap (the value is negative when the node move downward (Fig. 6)):

$$F_{i,a} = \pm k_c \bullet l_{av,i} \bullet d_b \bullet d_{gap}/2 \tag{19}$$

where d_{gap} is the gap value, and is equal to the difference between the bolt hole diameter and the one of bolt.

Since the deformation of the bolt and bolt hole on both sides of the joint is symmetrical, the moment in the bolt on the joint is equal to zero, and the shear force V_{apply} is applied on the midpoint A (Fig. 6b), where V_A is equal to the total shear force F_{total} divided by the bolt number m, $V_A = F_{total}/m$. The type of constraint at the endpoint O (Fig. 6b) influences significantly the bolt deformation (the effects of the constraints are discussed in the next section).

Based on the shear deformation model (Fig. 6b), the equivalent shear stiffness of the circular joint can be obtained by the following equation:

$$(k \bullet G \bullet A_J)_{eq} = \frac{m \bullet \Delta V_A \bullet L_b}{2 \bullet \Delta v_A} \tag{20}$$

where v_A is the transversal displacement in the midpoint node A, $v_A = v_{n+1}$, m is number of the bolts.

3.2. Analysis of the critical parameters that influence the behaviour of the bolts in circular joints

Based on a real case (Zuo et al., 2022), the straight bolt deformation is calculated under the application of a shear force on the circular joint of the segmental lining. The assumed diameter of the bolt is 30 mm and its length is 0.52 m. 16 bolts are located around the circumferential joint. The mechanical parameters of the bolt are: 206000 MPa and 0.3 for the steel elastic modulus and Poisson's ratio. The shear stiffness of the bolt is 49.64MN. The elastic modulus of concrete is assumed 34500 MPa, and the Poisson's ratio is 0.167. The gap between the hole wall and the bolt is 5 mm.

(1) the bolt deformation and the forces distribution along the bolt and the effect of the constraint type at the endpoint O

Due to the presence of the nut and the plate at the endpoint O, three different movement types may be observed. Therefore, the application of the three different constraints on the endpoint O are considered: no transversal displacements and no rotations ($v = 0, r = 0$), no rotations and transversal displacements free ($r = 0$), no constraints at the endpoint O (*free*). The transversal displacements, rotations, shear forces and moments along the bolt are shown in Fig. 7 to Fig. 10 when the total shear force acting on the circular joint is 5MN (the shear force acting on each bolt is 0.3125MN). The bolt is divided in the numerical model into 30 elements.

Due to the movement of the bolt in the transversal direction (perpendicularly to the bolt axis) near the endpoint O and the midpoint

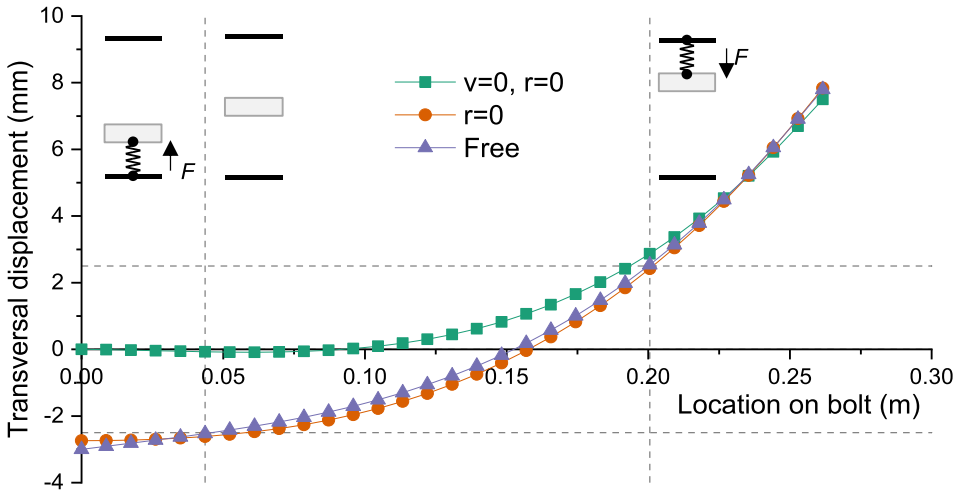

Fig. 7. Transversal displacements of the bolt along its axial direction under the application of a shear force (transversal force) of 0.3125MN in the midpoint A on the circular joint. The dotted lines allow to identify the zones near the endpoint O and the midpoint A where the contact between the bolt and the hole wall is reached in the case of constraint type *free*.

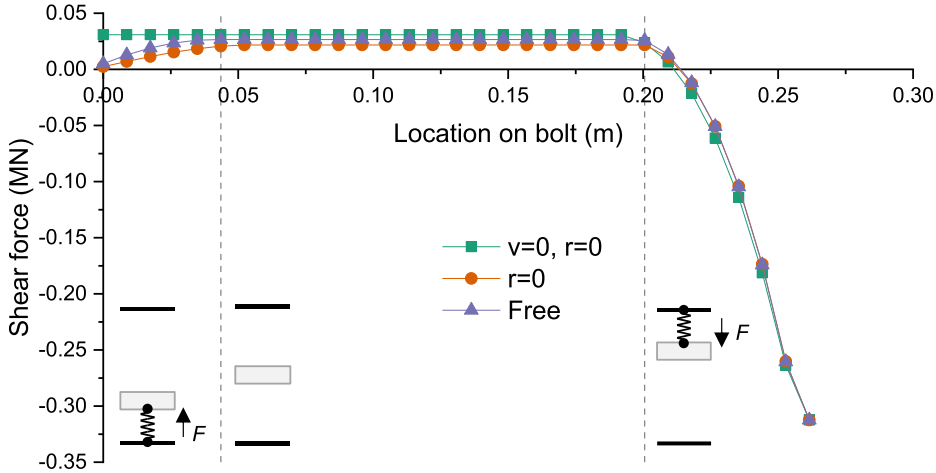

Fig. 8. Shear force of the bolt along its axial direction under the application of a transversal force of 0.3125MN in the midpoint A on the circular joint. The dotted lines allow to identify the zones near the endpoint O and the midpoint A where the contact between the bolt and the hole wall is reached in the case of constraint type *free*.

A, the hole wall is compressed (bolt goes into contact with the hole wall). Due to the type of constraint at the endpoint, the compressed hole wall zones are different: for $v = 0, r = 0$ constraint type the bolt nodes at the contact are 24–31, which is the node number from 0 on endpoint O to 31 on the midpoint A; for $r = 0$ constraint type are 1–7 and 25–31; for *free* constraint type are 1–6 and 24–31. From Fig. 7 it is possible to see how the transversal displacements of the bolt near the endpoint *O* can have a great difference on the basis of the type of constraint, while they are similar near the midpoint *A*. The maximum value of the shear forces in the bolt is reached at the midpoint *A* (Fig. 8). The ratio between the applied shear force on the circular joint (in the midpoint A) and the obtained transversal relative displacements of segments in the same point (obtained by the transversal displacement of the bolt in point A) permits to obtain the shear stiffness of the circular joint.

Rotations of the bolt (Fig. 9) show an increasing trend from the endpoint O to the midpoint A. The moments increase from the endpoint and reach a negative peak value at a certain distance from the midpoint A (Fig. 10). The constraints have a significant influence on the value of rotations and moments: the constraint type $v = 0, r = 0$ has the minimum value of the rotation at the midpoint A among the three constraint types, but it has the maximum positive moment at the endpoint (Fig. 10).

In order to know the relationship among the shear force acting on the circular joint, the relative transversal displacement of the lining rings (which is equal to 2 times the bolt displacement at the midpoint A) and the shear stiffness of the circular joint (calculated by Eq. (20)), the graphs of Figs. 11 and 12 are shown.

The shear force is very small when the relative transversal displacement is lower than the gap between the hole wall and the bolt, and it increases noticeably after the gap. Although the differences of the shear force in Fig. 11 are small among different constraints, the shear stiffness shows an obvious difference (Fig. 12). Due to the large degrees of freedom of the system when the relative transversal displacement of segments is smaller than the gap, the equations with the constraints types of $r = 0$ and *free* cannot be solved, and only the one with the $v = 0, r = 0$ constraint type can be calculated (Figs. 11 and 12).

The shear stiffness has a rapid increase when the relative displacement is larger than the gap. When the relative transversal displacement

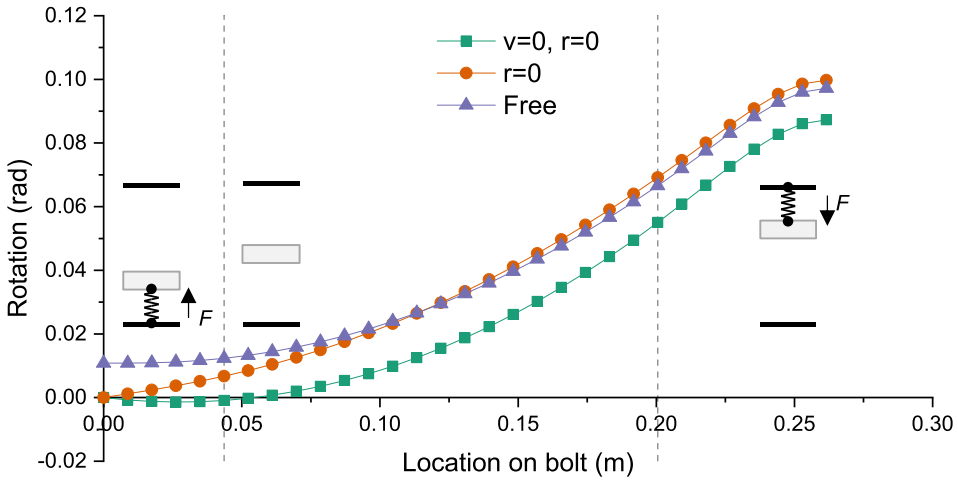

Fig. 9. Rotations of the bolt along its axial direction under the application of a transversal force of 0.3125MN in the midpoint A on the circular joint. The dotted lines allow to identify the zones near the endpoint O and the midpoint A where the contact between the bolt and the hole wall is reached in the case of constraint type *free*.

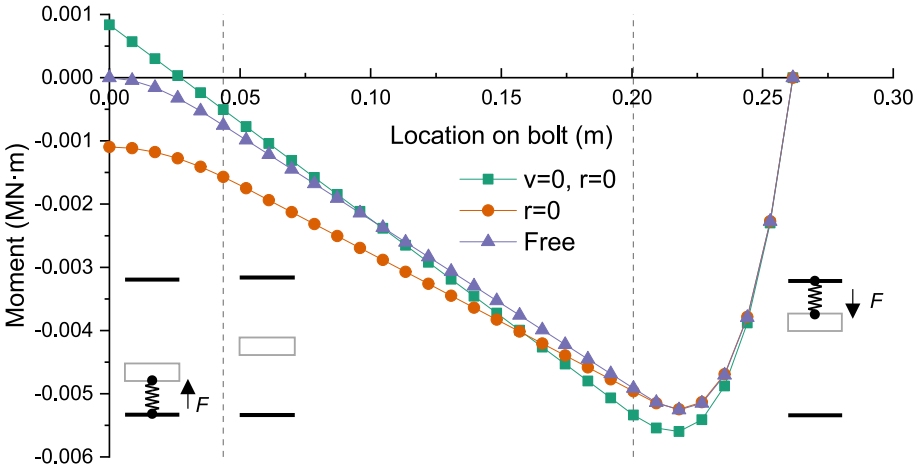

Fig. 10. Moments of the bolt along its axial direction under the application of a transversal force of 0.3125MN in the midpoint A on the circular joint. The dotted lines allow to identify the zones near the endpoint O and the midpoint A where the contact between the bolt and the hole wall is reached in the case of constraint type *free*.

is larger than 10 mm, the values of the shear stiffness of the circular joint tend to be the same varying the type of constraint.

Based on Eq. (1), the shear stiffness (49.64 MN) of the circular joint results to be overestimated with respect to that one that can be obtained by the detailed analysis shown in this section.

(2) Concrete foundation modulus

Based on Eq. (7) and Eq. (8), the concrete foundation modulus k_c are obtained, and are equal to 74.87 MPa/mm (Eq. (7)) and 96.15 MPa/mm (Eq. (8)), respectively. The comparison between the shear stiffnesses calculated from these different k_c values are shown in Fig. 13.

From Fig. 13 it is possible to see how the increase of the concrete foundation modulus causes the improvement of the shear stiffness of the joint when the bolt reaches the contact with the hole wall. The results shows that the consideration of the contact between the bolt and the hole wall is very important for the determination of the shear stiffness of the segmental lining joint; on the other hand, it is proved that the concrete foundation modulus is the key parameters to resolve the shear stiffness of the joint. From Eq. (7) and Eq. (8), the concrete foundation modulus is influenced by the compressive strength of the concrete and the diameter of bolt. Although the concrete foundation modulus is very important, there is a few tested results in the literatures, where Soroushian et al. (1987) test the value for the conventional concrete, and Khazaeeu and Ghalehnovi (2018) test the one for the ultra-high performance concrete (UHPC). From the experimental results of Soroushian et al. (1987), the empirical equation (Eq. (7)) is widely used by the researches (Caggiano et al., 2012; El-Ariss, 2007; He and Kwan, 2001; Prates Aguiar and Barreto Caldas, 2022; Sørensen et al., 2017). This paper focus on the development of an evaluation method for the shear stiffness of joint, and the Eq. (7) is adopted. However, a more detailed evaluation for the concrete foundation modulus based on a series of the experimental results is significant and valuable.

Furthermore, in order to improve the joint shear stiffness and reduce the dislocation between the adjacent segmental rings, a high strength concrete or a special structure with a high concrete foundation modulus around the bolt hole can be adopted; experimental tests should be developed in order to understand the effective improvement in k_c and in the shear stiffness of the joint for each special structure foreseen for this purpose.

4. The effect of the geometry and shape of the bolt on the mechanical behaviour of the circular joint

The shape of the bolt is not always straight (Fig. 5); inclined bolts and curved ones are widely used in tunnel engineering (Feng et al., 2018; Liu et al., 2020c). Therefore, the model which can be used to calculate the shear deformation of a curved bolt needs to be developed to be able to analyse the actual shape of the bolt.

Although the shape of the bolt and the bolt hole is symmetrical, the curved bolt is not symmetrical after its deformation, and the total bolt (from node O to node B) needs to be simulated in the model (Fig. 14). Based on the model of Fig. 14, the shear force can be obtained when the right segment develops a transversal displacement v_{seg}.

Since the local stiffness matrix is more conveniently based on the local Cartesian reference system and the global matrix is generally based on the global one, a transformation of the reference system is necessary. The element stiffness matrix on the global Cartesian reference system is represented by the following equation:

$$[K_b]_i = \begin{bmatrix} C^2\bullet\frac{EA}{l}+S^2\bullet\frac{12EI}{(1+\Phi)l^3} & CS\bullet\frac{EA}{l}-CS\bullet\frac{12EI}{(1+\Phi)l^3} & -S\bullet\frac{6EI}{(1+\Phi)l^2} & -C^2\bullet\frac{EA}{l}-S^2\bullet\frac{12EI}{(1+\Phi)l^3} & -CS\bullet\frac{EA}{l}+CS\bullet\frac{12EI}{(1+\Phi)l^3} & -S\bullet\frac{6EI}{(1+\Phi)l^2} \\ CS\bullet\frac{EA}{l}-CS\bullet\frac{12EI}{(1+\Phi)l^3} & S^2\bullet\frac{EA}{l}+C^2\bullet\frac{12EI}{(1+\Phi)l^3} & C\bullet\frac{6EI}{(1+\Phi)l^2} & -CS\bullet\frac{EA}{l}+CS\bullet\frac{12EI}{(1+\Phi)l^3} & -S^2\bullet\frac{EA}{l}-C^2\bullet\frac{12EI}{(1+\Phi)l^3} & C\bullet\frac{6EI}{(1+\Phi)l^2} \\ -S\bullet\frac{6EI}{(1+\Phi)l^2} & C\bullet\frac{6EI}{(1+\Phi)l^2} & \frac{(4+\Phi)EI}{(1+\Phi)l} & S\bullet\frac{6EI}{(1+\Phi)l^2} & -C\bullet\frac{6EI}{(1+\Phi)l^2} & \frac{(2-\Phi)EI}{(1+\Phi)l} \\ -C^2\bullet\frac{EA}{l}-S^2\bullet\frac{12EI}{(1+\Phi)l^3} & -CS\bullet\frac{EA}{l}+CS\bullet\frac{12EI}{(1+\Phi)l^3} & S\bullet\frac{6EI}{(1+\Phi)l^2} & C^2\bullet\frac{EA}{l}+S^2\bullet\frac{12EI}{(1+\Phi)l^3} & CS\bullet\frac{EA}{l}-CS\bullet\frac{12EI}{(1+\Phi)l^3} & S\bullet\frac{6EI}{(1+\Phi)l^2} \\ -CS\bullet\frac{EA}{l}+CS\bullet\frac{12EI}{(1+\Phi)l^3} & -S^2\bullet\frac{EA}{l}-C^2\bullet\frac{12EI}{(1+\Phi)l^3} & -C\bullet\frac{6EI}{(1+\Phi)l^2} & CS\bullet\frac{EA}{l}-CS\bullet\frac{12EI}{(1+\Phi)l^3} & S^2\bullet\frac{EA}{l}+C^2\bullet\frac{12EI}{(1+\Phi)l^3} & -C\bullet\frac{6EI}{(1+\Phi)l^2} \\ -S\bullet\frac{6EI}{(1+\Phi)l^2} & C\bullet\frac{6EI}{(1+\Phi)l^2} & \frac{(2-\Phi)EI}{(1+\Phi)l} & S\bullet\frac{6EI}{(1+\Phi)l^2} & -C\bullet\frac{6EI}{(1+\Phi)l^2} & \frac{(4+\Phi)EI}{(1+\Phi)l} \end{bmatrix} \tag{21}$$

where C is $\cos\alpha_i$, S is $\sin\alpha_i$, α_i is the angle between the bolt element and the horizontal axis, it also represents the angle between the local Cartesian reference system and the global one (Fig. 15).

The sub matrix $[K_{i,a}]$ of the matrix $[K_b]_i$ is used to express the first nine elements; $[K_{i,b}]$, $[K_{i,c}]$ and $[K_{i,d}]$ can be obtained by the same way.

$$[K_{i,a}] = \begin{bmatrix} C^2\bullet\frac{EA}{l}+S^2\bullet\frac{12EI}{(1+\Phi)l^3} & CS\bullet\frac{EA}{l}-CS\bullet\frac{12EI}{(1+\Phi)l^3} & -S\bullet\frac{6EI}{(1+\Phi)l^2} \\ CS\bullet\frac{EA}{l}-CS\bullet\frac{12EI}{(1+\Phi)l^3} & S^2\bullet\frac{EA}{l}+C^2\bullet\frac{12EI}{(1+\Phi)l^3} & C\bullet\frac{6EI}{(1+\Phi)l^2} \\ -S\bullet\frac{6EI}{(1+\Phi)l^2} & C\bullet\frac{6EI}{(1+\Phi)l^2} & \frac{(4+\Phi)EI}{(1+\Phi)l} \end{bmatrix} \tag{22}$$

The global matrix $[K]_g$ can be derived based on the element stiffness matrix positioned along the diagonal of the matrix:

$$[K] = \begin{bmatrix} k_{1,a} & k_{1,b} & 0 & \cdots & 0 & 0 \\ k_{1,c} & k_{1,d}+k_{2,a} & k_{2,b} & \cdots & 0 & 0 \\ 0 & k_{2,c} & k_{2,d}+k_{3,a} & \cdots & 0 & 0 \\ \vdots & \vdots & \vdots & \ddots & \vdots & \vdots \\ 0 & 0 & 0 & \cdots & k_{n-1,d}+k_{n,a} & k_{n,b} \\ 0 & 0 & 0 & \cdots & k_{n,c} & k_{n,d} \end{bmatrix} \tag{23}$$

The external force on the node can be represented by the nodal displacements and the global matrix:

$$[F]_g = [K]_g \bullet [S]_g \tag{24}$$

where

$[F]_g$ is the matrix of the nodal force, $[F]_g = [F_1 \quad F_2 \quad F_3 \quad F_4 \quad \cdots \quad F_n \quad F_{n+1}]^T$; $[F_i]$ $(i = 1,2,3,\cdots,n+1)$ are the submatrix of the external forces on j th nodes which include the force $F_{X,j}$ along the X-axis, the force $F_{Y,j}$ along the Y-axis and the bending moment $F_{Z,j}$ of node j on the global Cartesian reference system, $[F_j] = [F_{X,j} \quad F_{Y,j} \quad F_{Z,j}]^T$.

$[S]_g$ is the matrix of the nodal displacements, $[S]_g = [S_1 \quad S_2 \quad S_3 \quad S_4 \quad \cdots \quad S_n \quad S_{n+1}]^T$; $[S_j]$ $(j = 1, 2, 3, \cdots, n+1)$ consist of the displacement $S_{X,j}$ along the X-axis, the displacement $S_{Y,j}$ along the Y-axis and the rotation angle $S_{Z,j}$ of node j on the global Cartesian reference system, $S_j = [S_{X,j} \quad S_{Y,j} \quad S_{Z,j}]^T$.

Let $[K_j]$ represent the submatrix along main diagonal on Eq. (23), such as $[K_1] = [K_{1,a}]$, $[K_n] = [K_{n-1,d} + K_{n,a}]$.

When considering the reaction force of the hole wall on the bolt, an additional term $[K_{c,j}]$ need to be considered in the submatrix $[K_j]$ of the global stiffness matrix $[K]_g$ along the diagonal: (Oreste, 2007):

$$[K_{c,j}] = \begin{bmatrix} K_{c,j}\bullet\cos^2\beta_j & K_{c,j}\bullet\sin\beta_j\bullet\cos\beta_j & 0 \\ K_{c,j}\bullet\sin\beta_j\bullet\cos\beta_j & K_{c,j}\bullet\sin^2\beta_j & 0 \\ 0 & 0 & 0 \end{bmatrix} \tag{25}$$

where $K_{c,j}$ is the reaction stiffness from the hole wall on the jth node, and can be calculated by the following equation:

$$K_{c,j} = k_c \bullet l_{av,j} \bullet d_b \bullet \sin(\beta_j - \alpha_{i-1}) \tag{26}$$

where $l_{av,j}$ is the average length of the element around the jth node, $l_{av,j} = (l_{i-1} + l_i)/2$, l_i is the length of the ith element, β_i is the angle of the spring with the horizontal axis (Fig. 15), and can be calculated by the following equation.

$$\beta_j = \frac{\alpha_{i-1}}{2} + \frac{\alpha_i}{2} + \frac{\pi}{2} \tag{27}$$

For the 1st and n+1th node, the angle of the spring and the reaction force can be obtained based on the adjacent elements: $\beta_1 = \alpha_1 + \pi/2$, $F_{c,1} = k_c \bullet l_1 \bullet d_b/2$, $\beta_{n+1} = \alpha_n + \pi/2$, $F_{c,n+1} = k_c \bullet l_n \bullet d_b/2$.

In addition to the displacement boundary conditions illustrated in

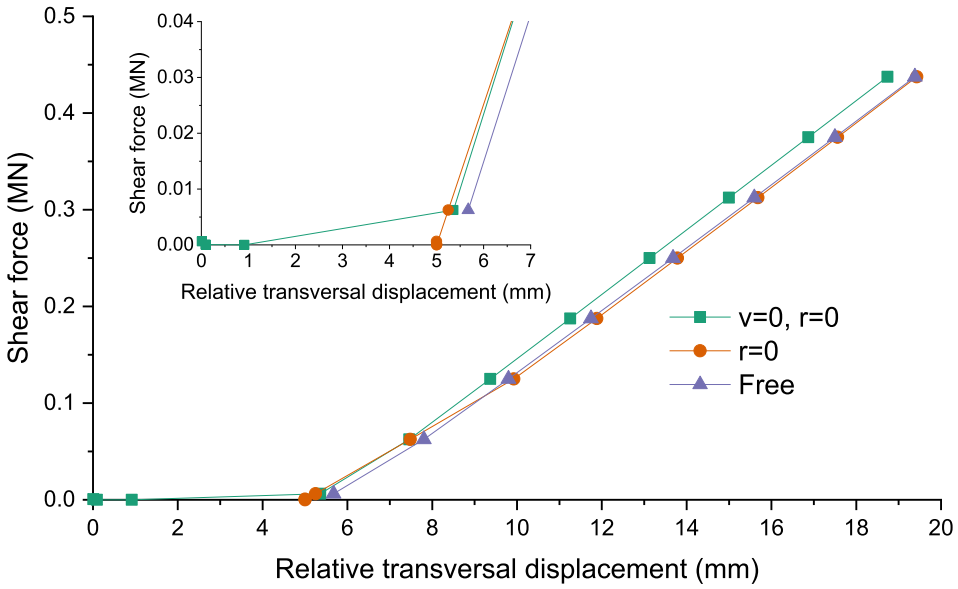

Fig. 11. Force-displacement law of the circular joint with different constraints on the bolt endpoint: correlation between relative transversal displacements and shear forces acting on the circular joint.

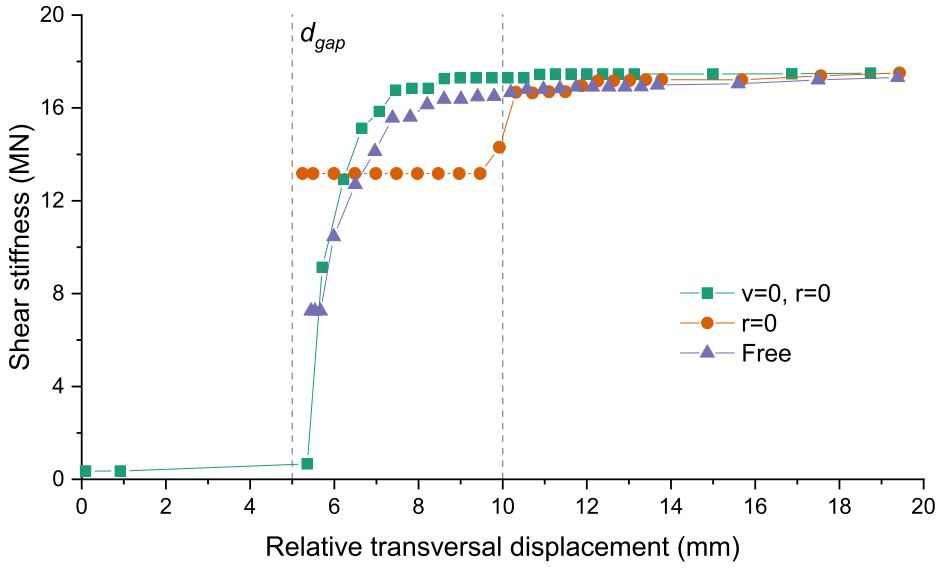

Fig. 12. Shear stiffness of the circular joint with different constraints on the bolt endpoint, varying the relative transversal displacement.

the previous section, a specific constrain of the nut and plate along the bolt axial direction at the two endpoints of the bolt (O and B), must be foreseen.

Since a constrained force from nut and plate is relied on the nodal displacement, additional stiffness matrixes $[K_{e,O}]$ and $[K_{e,B}]$ need to be added separately to the first submatrix and to the last one $[K_j]$, where j is equal to 1 and $n+1$. $[K_{e,O}]$ can be obtained by the following equation, and $[K_{e,B}]$ can be derived in the same way:

$$[K_{e,O}] = \begin{bmatrix} K_{e,O} \bullet \cos^2\alpha_1 & K_{e,O} \bullet \sin\alpha_1 \bullet \cos\alpha_1 & 0 \\ K_{e,O} \bullet \sin\alpha_1 \bullet \cos\alpha_1 & K_{e,O} \bullet \sin^2\alpha_1 & 0 \\ 0 & 0 & 0 \end{bmatrix} \tag{28}$$

where α_1 is the angle of the first element (Fig. 15), $K_{e,O}$ is the reaction stiffness from the end surface at the node O, which is compressed by the plate on the bolt head, and can be calculated by the following equation:

$$K_{e,O} = k_c \bullet \frac{\pi}{4} \bullet \left(d_{plate}^2 - d_h^2\right) \tag{29}$$

where d_{plate} is the diameter of the plate, d_h is the diameter of the bolt hole, which is equal to $d_b + d_{gap}$.

During the installation of segments and bolts, a pretension force F_{pre} is applied on each bolt. Therefore, the additional force vector $[F_{pre,j}] = [F_{preX,j} \quad F_{preY,j} \quad 0]^T$ should be added to the nodal force vector, where $F_{preX,j}$ and $F_{preY,j}$ can be obtained by the following equation:

$$F_{preX,j} = \pm F_{pre} \bullet \cos(\alpha_j) \tag{30}$$

$$F_{preY,j} = \pm F_{pre} \bullet \sin(\alpha_j) \tag{31}$$

where the pretension force is negative for the node O, and positive for the node B.

Based on the bolt shear deformation model (Fig. 14), the shear force

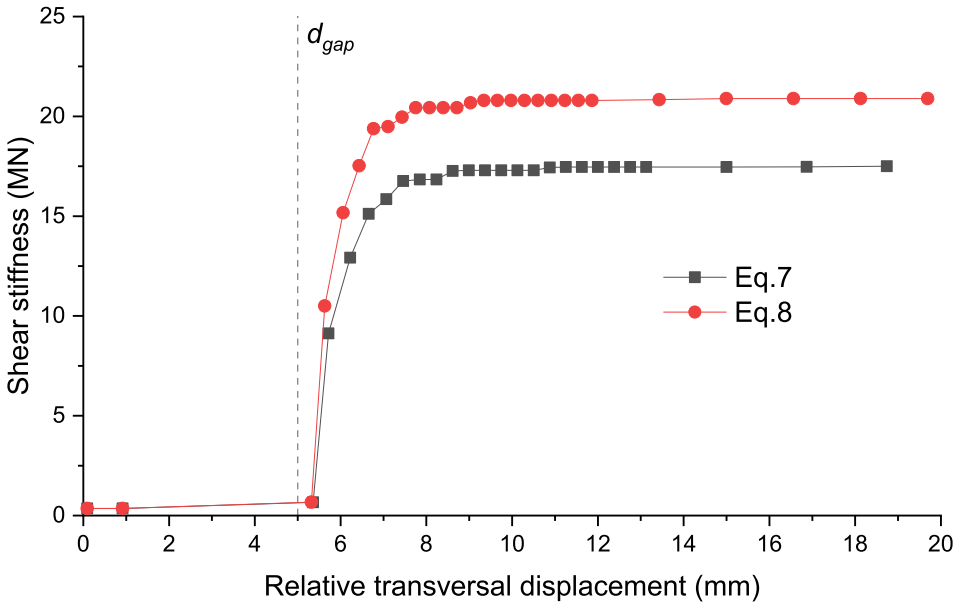

Fig. 13. The shear stiffnesses of a circular joint varying the relative transversal displacement of the lining segments with different concrete foundation modulus k_c.

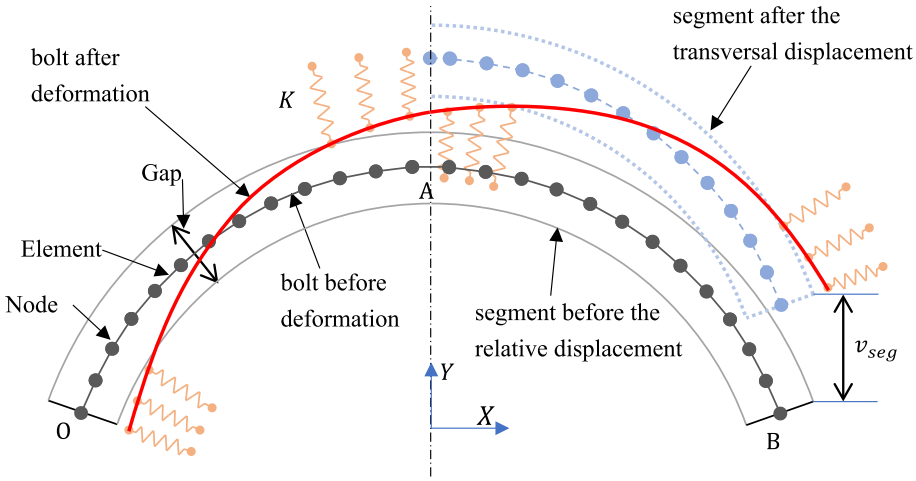

Fig. 14. The bolt deformation under the application of a shear force to the segment on the right side of the picture.

at the midpoint A (V_{bolt}) of the bolt can be obtained: it is the maximum shear force along the bolt, when one segment has a relative transversal displacement v_{seg} with respect to the other one.

Considering the influence of the friction on the circular joint, the limit friction force (V_{fri}) can be obtained by the following equation:

$$V_{fri} = N \bullet \tan(\varphi) \tag{32}$$

where φ is the friction angle on the joint, N is the normal force acting on the joint.

Therefore, the equivalent shear stiffness of the joint can be obtained by the following equation:

$$(k \bullet G \bullet A_J)_{eq} = \frac{\Delta\left(V_{fri} + m \bullet V_A + V_{tenon}\right) \bullet L_{bp}}{\Delta v_{seg}} \tag{33}$$

where V_{tenon} is the shear force acting on the tenon, L_{bp} is the projection length of the curved bolt along X-axis.

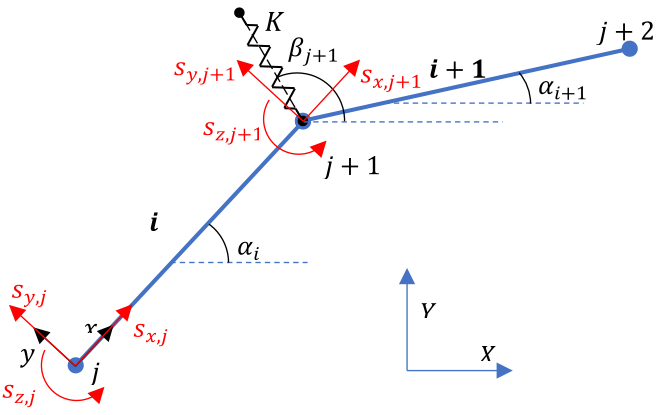

Fig. 15. The relationship between the elements of the numerical model and the spring simulating the reaction force by the concrete on the hole wall applied to a node of the bolt. Key: s_x, s_y, s_z are nodal displacements in the local coordinate system.

5. Examples of the evaluation of the circular joint shear stiffness by the developed numerical model

5.1. The deformation of a curved bolt, the force distribution along its axis and the effect of the constraint at the endpoints, varying the relative transversal displacement of segments

The deformation of a curved bolt is obviously influenced by the axial force on the endpoint of the bolt; for this reason the situation is different from the straight bolt model, for which the axial force is neglected during the stress-strain state analysis. The constraints on the endpoint are divided into 4 different types, listed in Table 2.

The basic parameters adopted in the calculation examples are based on a project where a shield TBM machine was used in a tunnel under the Yangtze river in China (Wang, 2020; Zuo et al., 2022); the geometrical and mechanical parameters of the segmental lining and the bolts are listed in Table 3 and Table 4. Based on the Standard from China, 2021, the minimum diameter of the bolt hole is about 33–36 mm. The gap between the bolt and the bolt hole is considered 5 mm. The bolt is divided into 61 numerical elements (30 elements in the right segment and 30 elements in the left one, while 1 element simulates the circular joint). The elastic deformation of the bolt and the concrete is analysed when the segments have a relative transversal displacement of 8 mm; the displacements and internal forces are shown from Fig. 16 to Fig. 21.

When the segments have a transversal relative displacement along the circular joint, the transversal displacements of the bolt along the axial direction increase. In Fig. 16b, the displacements on the left segment along the transversal direction of the bolt are positive and increase from the endpoint to the midpoint; the displacements on the right segment have an opposite direction (the trend is similar with the one of the straight bolt in Fig. 7).

Due to the influence of the constraint at the endpoint of bolt, the length and location of the compressed zones have some differences: the constraint (No spring) does not have any compressed zones; the node numbers of the compressed zones for the constraint type ($x = 0$, $y = 0$, $r = 0$) and ($x = K_e$, $y = 0$, $r = 0$) are from 26 to 37; for the constraint type ($x = K$, y free, $r = 0$) from 28 to 35; for the constraint type ($x = K_e$, y & r free) are nodes 1, 2, from 27 to 36, 61 and 62. The marker lines of the nodes 27 and 36 of the bolt are shown in the figures from Fig. 16 to Fig. 21. Compared with the Case 0 (Fig. 16), the transversal displacements of Case 1 (C1) and Case 2 (C2) are the same of the Case 0 (C0) at the endpoints and in the midpoint; however, the compressive forces from the hole wall limit the deformation of the bolt.

From Fig. 17, it is possible to see how the compressive forces from the hole wall lead to a significant increase of the bolt shear force in the midpoint, and the absence of constraint in the endpoints along the transversal direction (Case 3 and Case 4) causes a smaller shear force in the midpoint than for the restricted deformation cases (Case 1 and Case 2). From Figs. 16 and 17, we can note that the constraints on the rotation at the endpoints (comparison between Case 3 and Case 4) has a minimum influence on the transversal displacements and also on the maximum shear force in the bolt.

From Fig. 18, it is possible to note how for Case 0 (the concrete hole wall doesn't influence the bolt deformation) the bolt has negative displacements along its axis (local reference system) and reach a maximum value at the midpoint where segments have a relative transversal displacement. The type of constraint at the endpoint and the reaction of the concrete on the hole wall significantly influence the trend of the axial displacements along the bolt. In Fig. 19, the axial force of the Case 0 has the maximum value at the endpoints and is equal to 0 in the midpoint; the bolt is compressed on the right segment and is stretched on the left segment, in function of the type of relative transversal displacement of the segments. When reaction forces are applied on the bolt by the hole wall (Case 1), the maximum axial displacement decreases, and the maximum axial force can be observed on the dividing line between the compressed and uncompressed zone. Considering the deformation along the axial direction (Case 2), there are positive axial displacements at the two endpoints, and the whole bolt is stretched, with a trend of the axial force along the bolt parallel to that of Case 1. Furthermore, the absence of any constraints for the transversal displacement and the rotation at the endpoints (Case 4) leads to positive axial displacements (local reference system) along the bolt and near a nil value at the midpoint. Due to the absence of constraints at the endpoints (Case 4), the axial force at the endpoint is close to 0 and the maximum value of the axial force is smaller than for the other examined cases. When only the rotation is prevented (Case 3), the bolt has everywhere positive axial displacements; in this case the axial force tends to be 0 in the uncompressed zone of the right segment, and the maximum axial force is reached at the right endpoint.

Based on the developed analyses, the constraints type of Case 2 produces the maximum axial force (at the dividing line, node N27), which should be considered in order to verify the ability of the bolt to withstand the induced stresses inside it without yielding.

Compared with the standard case (Case 0), the compressive forces which are applied by the hole wall (Case 1 and 2), cause the increasing of the maximum rotation which is reached near the joint (Fig. 20), and move the maximum moment from the endpoints (Case 0) to the dividing lines of nodes N27 and N36 (Case 1 and 2) (Fig. 21). The moment for Case 4 is equal to 0 at the endpoints and the maximum value is smaller than for Case 1 and 2. When the rotation is restricted (Case 3), a significant increase of the moment at the endpoints is detected; the moments of the bolt on the right segment in the uncompressed zone are constant, and the ones on the left segment in the uncompressed zone have an opposite trend compared with other types of constraint.

On the basis of the performed analyses, the maximum shear force of each constraint type is reached at the midpoint, and the constraint of the transversal displacements (Case 1 and Case 2) leads to a higher maximum shear force. The maximum value of moments and shear forces are located at the dividing line when the endpoints are restricted (Case 1, 2, 4), while are located at the endpoints when the transversal displacements are not constrained (Case 3).

When the right segment does not move and the left segment has a relative transversal relative movement, the corresponding maximum shear forces and the relative displacements of the segment are shown in Fig. 22: the slope of the graph represents the shear stiffness of the joint. The calculated values of the shear stiffnesses of the circular joint have been obtained and are shown in Fig. 23, varying the relative transversal displacements, considering only the contribution of the bolts and neglecting the influence of the friction and of the tenons.

The graph of the maximum shear force of the joint varying the relative transversal displacement can be divided into two main sections, based on the gap between the bolt and the hole wall: when the displacement is lower than the gap, small and slowly increasing shear forces are detected; for displacements greater than the gap, high and rapidly increasing shear forces can be observed. Due to the low number of constraints, the shear force couldn't be obtained from the numerical model when the relative displacement is smaller than the gap for Case 3 and 4. From Fig. 23, the increase of the shear stiffness with the relative displacement can be divided into three phases: a) very low stable phase when the displacement is lower than the gap (the shear stiffness is very low); b) the increasing phase for displacements greater than the gap (the shear stiffness grows with the increase of the relative displacement); c) the high-stable phase (the shear stiffness reaches its maximum value). In the second phase, the shear stiffness for Case 4 is smaller than the ones of Case 1 and 2; and the shear stiffness of Case 3 results to be constant when the relative displacement is smaller than 8 mm and the bolt near the endpoints does not come in contact with the hole wall.

Compared with the straight bolt, of which the length is equal to the projection length of the curved bolt, the maximum shear stiffness of the curved bolt (13.7MN on Fig. 23) is smaller than the one of the straight bolt (17.5MN on Fig. 12), but the increasing trends of the shear stiffness with the relative transversal displacement are similar. It means that the

Table 2
Constraint types on the endpoint of the curved bolt considered in the study.

Case No.	Displacement axial direction	Displacement transversal direction	Rotation	Sign
0	0	0	0	No springs (C0)
1	0	0	0	x = 0, y = 0, r = 0 (C1)
2	K_e	0	0	x = K_e, y = 0, r = 0 (C2)
3	K_e	Free	0	x = K_e, y free, r = 0 (C3)
4	K_e	Free	Free	x = K_e, y & r free (C4)

where K_e means that the constrained force along the axial direction is applied on the bolt head (ending point) considering an axial stiffness in that point; Free means that there are no constraints on the endpoint of the bolt; 0 means that the endpoint is fixed along that direction and no displacement is permitted.

curved bolt has a greater relative transversal displacement than the straight bolt under the same applied shear force, and the curved bolt joint is softer than the straight bolt one due to weaker restrictions on both endpoints along the direction parallel to the joint.

During the installation, an axial pretension on the bolt is often applied at the endpoints, increasing the axial forces along the bolt and restricting displacements at the endpoints. Therefore, the type of constraints of Case 2 can be adopted to analyses the bolt deformation and the shear stiffness of the circular joint, when a bolt pretension is adopted.

5.2. The yielding of the bolt and of concrete and the influence of the bolt pretension and the gap between the hole and the bolt

The acting stresses σ_{max} (maximum normal stress on the border of the bolt cross-section) and σ_{id} (the maximum ideal stress on the cross- section axis) in the bolt can be determined by the axial force $N_{x'}$, the moment $M_{x'}$ and the shear force $T_{x'}$.

$$\sigma_{max} = \frac{4}{\pi \bullet d_b^2} \bullet N_{x'} + \frac{32}{\pi \bullet d_b^3} \bullet M_{x'} \tag{34}$$

$$\sigma_{id}^2 = \left(\frac{4}{\pi \bullet d_b^2} \bullet N_{x'}\right)^2 + 3 \bullet \left(\frac{16}{3 \bullet \pi \bullet d_b^2} \bullet T_{x'}\right)^2 \tag{35}$$

Based on the Von-mises criteria, the yielding condition of the bolt can be defined by the following equation:

$$\sigma_y \leq \sigma_{ten} \tag{36}$$

where σ_y is the yielding stress of steel, σ_{ten} is the maximum tensile stress and can be obtained by the equation: $\sigma_{ten} = \max(\sigma_{max}, \sigma_{id})$.

For the limit stress of the concrete, Vintzēleou and Tassios (1986) divided the damage model of the concrete into model A and model B, described before. Therefore, the maximum compressive stress of the concrete in the limit condition can be determined by the following equation:

$$f_{cc}^* = \min\left(f_{cc,A}^*, f_{cc,B}^*\right) \tag{37}$$

where the $f_{cc,A}^*$ is the maximum compressive stress of the concrete when the concrete damage follow the model A, which can be calculated based on the equation proposed by Vintzēleou and Tassios (1986):

$$f_{cc,A}^* = 5 \bullet f_{cc} \tag{38}$$

where the $f_{cc,B}^*$ is the one for the model B, Soroushian et al. (1986) suggested the following equation based on a test result:

$$f_{cc,B}^* = 37.6 \bullet \frac{\sqrt{f_{cc}}}{\sqrt[3]{d_b}} \tag{39}$$

Table 3
Geometrical and mechanical parameters of the segmental lining ring.

External Diameter of tunnel	Internal Diameter of tunnel	Average Width of the ring	Concrete class	Elastic modulus of concrete	Passion's ratio
7.6 m	6.8 m	1.5 m	C60	34.5 MPa	0.167

Considering the influence of the pretension and the gap, the maximum shear force, tensile stress of the bolt and compressive stress of concrete are obtained considering the type of constrain of Case 2 (Figs. 24 and 25). The basic parameters of the example are the same of Sect. 5.1 (yielding stress of the bolt 640 MPa, compressive strength of concrete 60 MPa). In the calculation example the gap is considered 5 mm, the axial pretension of the bolt at the endpoints 0 MPa, and the relative transversal displacement of the segments 8 mm.

In Fig. 24, a small influence of the pretension on the maximum shear force of bolt and on the maximum compressive stress of the hole wall can be detected, while there is a significant influence on the maximum tensile stress σ_{ten} in the bolt. When the pretension is larger than 60 MPa, the tensile stress of the bolt overpasses the yielding stress (a critical case for the bolt). Therefore, a high pretension can lead to the bolt yielding; furthermore, the high pretension has a small influence on the bolt shear deformation, but it can increase the normal force on the joint improving the friction on the lining segment faces.

The gap between the bolt and the hole wall provides the space for the bolt deformation (Fig. 25): the maximum shear force in the bolt decreases with the increase of the gap, and the gap has a small influence on the maximum compressive stress of concrete on the hole wall. However, the maximum tensile stress σ_{ten} decreases initially varying the gap and then increases again when the gap is larger than 7 mm. In this case, the value of σ_{max} is larger than σ_{id}, and the maximum tensile stress in bolt depends on the axial force and the bending moment.

The increase of the gap can soften the bolt shear stiffness, but it can also cause an earlier yielding of the bolt when the gap is larger than a limit value. In order to know the influence of the gap, the shear stiffnesses with different gap values (0, 3, 5, 7 and 9 mm) were calculated based on the type of constraint of Case 2 (Table 1, Fig. 26). The shear stiffness is constant (14.18MN) when the gap is nil; the maximum shear stiffnesses in the third phase with different gap values tend to the same values (about 13.5MN). However, the length of the first and second phases is not the same, because it tends to be longer with the increase of the gap. Therefore, the increase of the gap can reduce the shear stiffness on a limited range of the relative transversal displacement between segments (in the first and second phases of the curve).

5.3. Comparison of the calculated results by the proposed numerical model with laboratory test results

During laboratory tests on a circular joint (Zuo et al., 2022), it was possible to determine the shear force necessary to guarantee an upward displacement of the left segment varying the applied normal force to the joint (Fig. 27); the measured values were compared with the calculated results by the proposed numerical model. The tested segments included not only the bolt but also a tenon (circular, with height 30 mm, diameter 105 mm, slope of lateral surfaces 72°, gap 5 mm) on the joint. The geometrical and mechanical parameters of the bolt and of segments are

Table 4
Geometrical and mechanical parameters of the curved bolt.

Type of bolt	Class of bolt	Diameter of bolt	Radius of curved bolt	Center angle of the bolt	No. of bolts in the joint	Elastic modulus of steel	Passion's ratio of steel	Yielding Strength of steel	Pretension stress of the bolt
M30	8.8	30 mm	380 mm	87°	16	206GPa	0.3	640 MPa	64 MPa

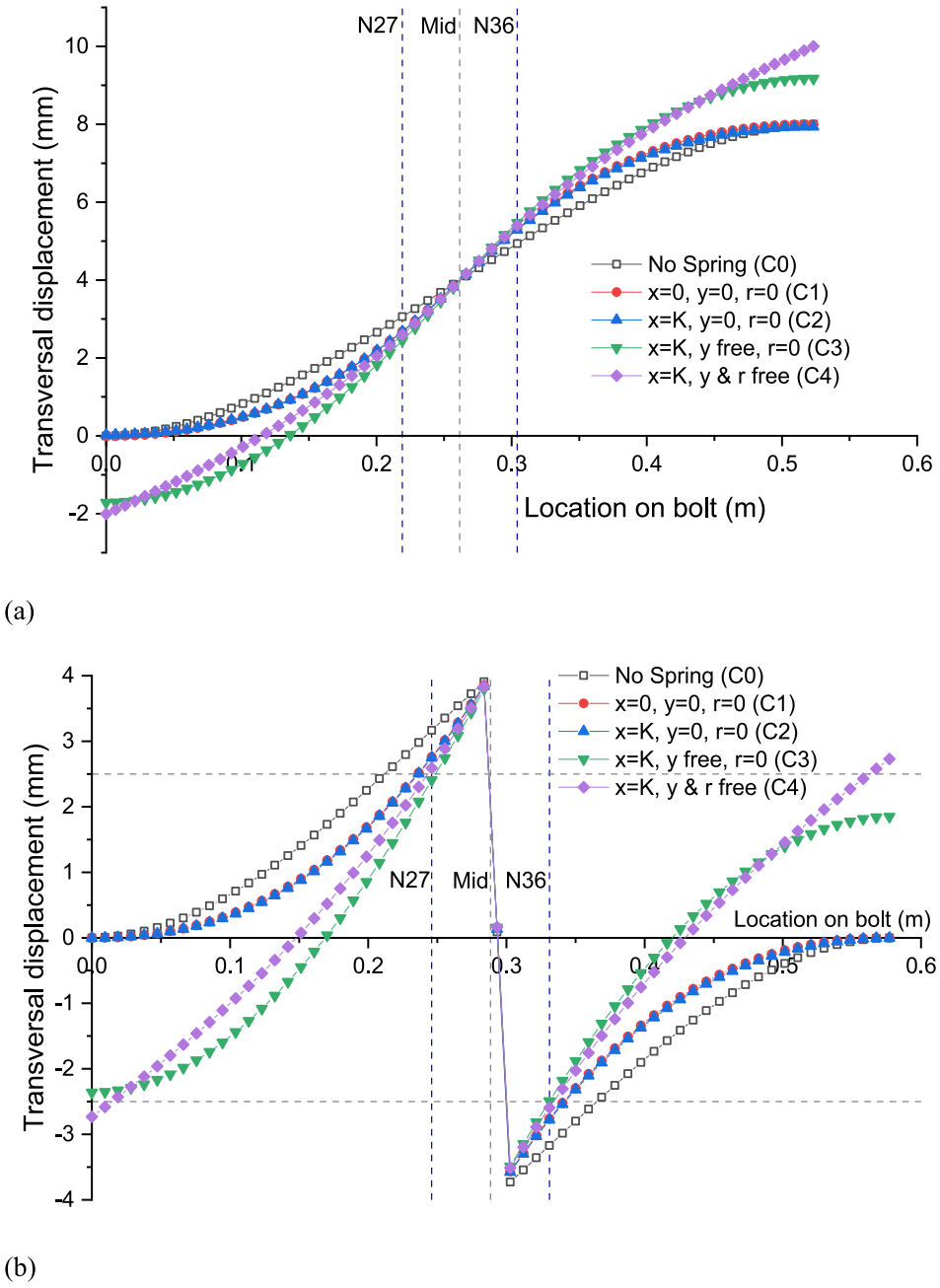

Fig. 16. The transversal displacement of the bolt along the axis direction. Key: (a) global reference system (x axis parallel to the tangent passing in the midpoint of the bolt, transversal displacement along y axis); (b) local reference system.

shown in Table 3 and Table 4. The numerical results (blue line) refer to a case with only a bolt without the tenon on the circular joint.

An initial sharp increase in the shear force during the laboratory tests (Fig. 27) can be referred to the presence of friction forces that depend on the applied normal force. Comparing the inclinations between the dotted red lines and the blue line it is possible to see a certain difference: it means a difference in the shear stiffness of the joint due to the presence of a tenon on the tested joint. The obtained shear stiffness by the numerical calculation without considering the presence of the tenon (21.88 kN/mm) is lower than the measured value by test results: 50 kN/mm for an applied force of 500 kN till to reach 100 kN/mm for an applied force of 2500 kN, where the value of shear stiffness is the slope of the curves in Fig. 27, which is equal to the equivalent shear stiffness of joint over the projection length of bolt based on Eq. (33).

In order to analyse the influence of the tenon on the developed laboratory tests, some interesting results from tenon shear tests by Xu

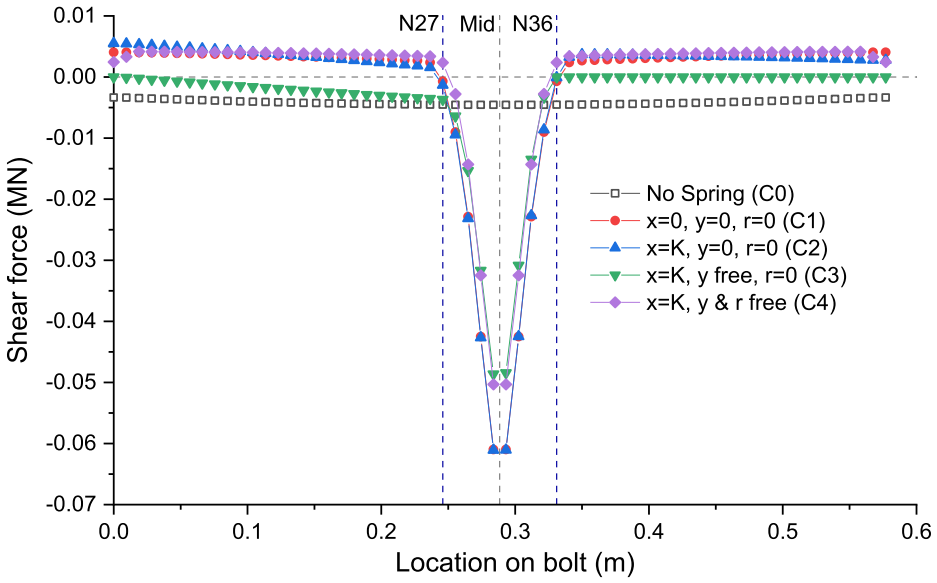

Fig. 17. The shear force in the bolt along the axis direction.

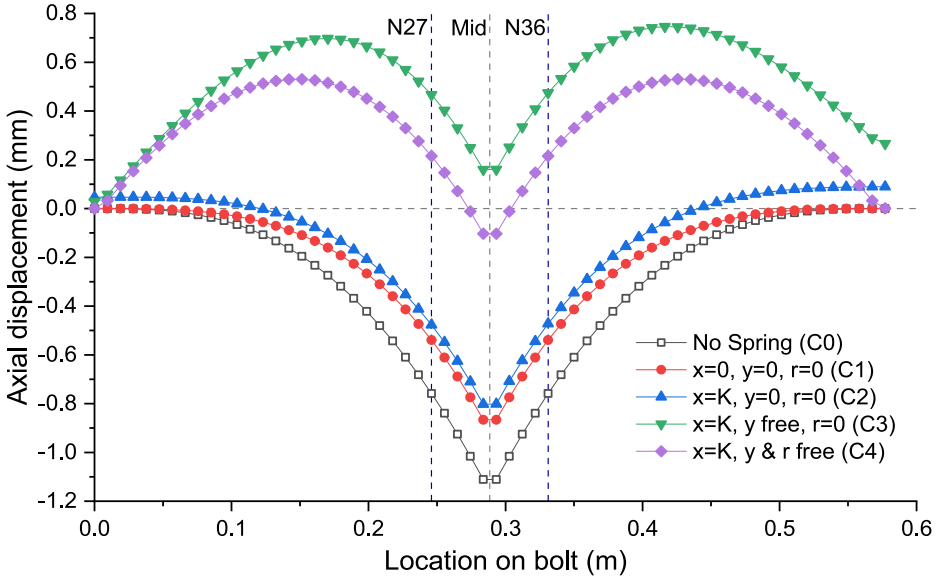

Fig. 18. The axial displacement of the bolt along the longitudinal direction (local reference system).

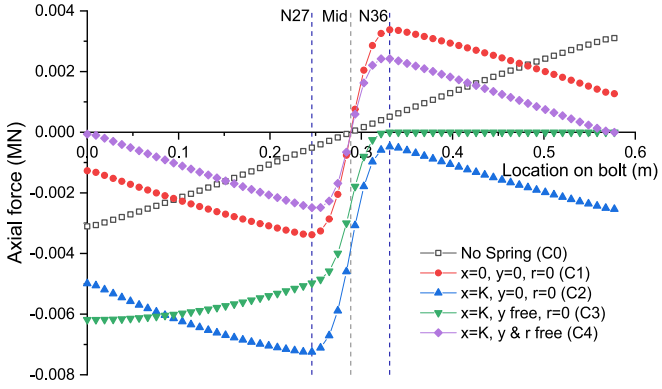

Fig. 19. The axial force along the bolt for different types of constraint at the endpoints. Key: the positive value of the axial force means a compressive force, the negative value a tensile force.

(2021) were considered. The shape of the tested tenons is rectangular plus two semicircles on the longer sides. The applied normal force is 200 kN. Depending on the shear direction, the tenon showed a shear stiffness value varying from 23 to 29 kN/mm (Xu, 2021), similar to the difference between the experimental results by Zuo et al. (2022) and the numerical ones. It means that the proposed numerical model is able to correctly determine the mechanical behaviour of the bolt during a relative transversal displacement of segments on the circular joints and also to evaluate with a certain precision the contribution of the bolt on the shear stiffness of the circular joint.

6. Conclusions

When the tunnel segmental lining has a deformation along the longitudinal direction under the application of the jack thrust, the slurry buoyancy and others construction loads, the circumferential joints have a weaker stiffness than the segmental lining rings. The evaluation of the bending and shear stiffnesses of these joints become a fundamental

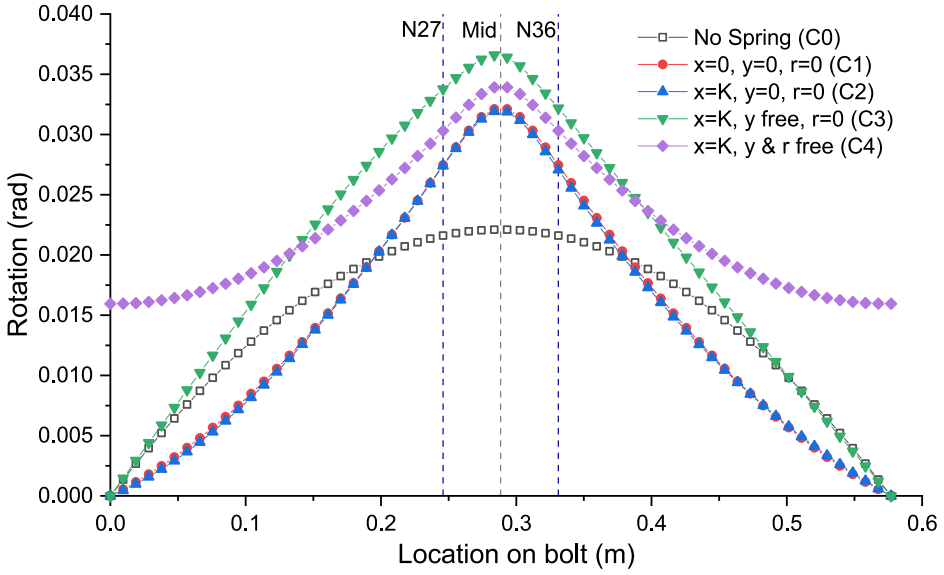

Fig. 20. The rotations of the bolt along its axial direction for the different types of constraint at the endpoints considered in the developed analyses.

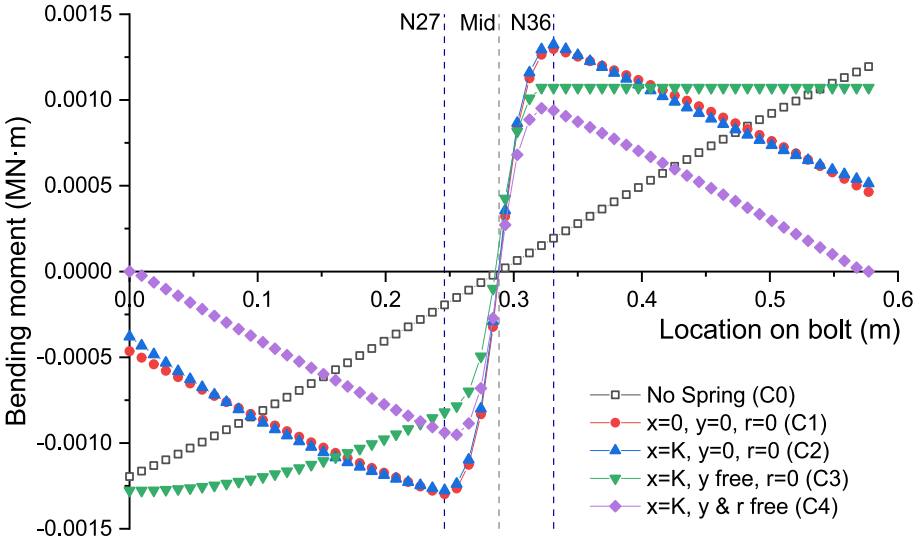

Fig. 21. The bending moments of the bolt along its axial direction for the different types of constraint at the endpoints considered in the developed analyses.

aspect for the design and the safety evaluation of the segmental lining. This paper mainly focuses on the evaluation of the shear stiffness of the circular joints.

The shear deformation process of the joint (shear force-shear displacement law) can be divided into three parts: a friction phase with a high shear stiffness, a shear deformation phase due to the presence of bolts and tenons along the circular joint, and a damage phase when the steel bolt yields or the concrete on the hole wall reaches its compressive strength. For the friction phase, the main influencing factors are the normal force and the friction angle on the concrete surfaces. Considering the shear deformation phase the bolt and the tenon can be analysed separately. By some specific experimental studies, the deformation characteristic of a tenon depends on its shape, height, width and lateral surfaces slopes; the mechanical behaviour of the bolt under a shear deformation along the circular joint relies on the stiffnesses of the bolt and the concrete on the hole wall and the tensile and compressive strength of steel and concrete, respectively.

In order to analyse in detail the bolt deformation under the constraints of the hole wall, a specific bolt shear deformation FEM model was developed based on the beam-spring approach. Considering the symmetry of the structure and loads, the half of the straight bolt was initially analysed. The constraints on the bolt endpoints were defined into three types based on the restrictions of the rotation and the transversal displacement. From the calculation results it was possible to see how the constraint types have an obvious influence on the bolt deformation along the bolt, while the effect of the constraint types on the transversal displacements, shear forces and moments at the circular joint is small.

From the proposed numerical model was also possible to evaluate the shear stiffness of the circular joint of the segmental lining, varying the relative transversal displacement between adjacent segments, considering the effect of the bolting system. The increase process of the shear stiffness due to the bolting system with the increase of the relative transversal displacements can be divided into three phases: initially a stable phase with a low and constant value, then an increasing phase with a grow of the shear stiffness varying the relative transversal displacement, finally a stable phase with a constant and large value when the whole bolt contacts the hole walls.

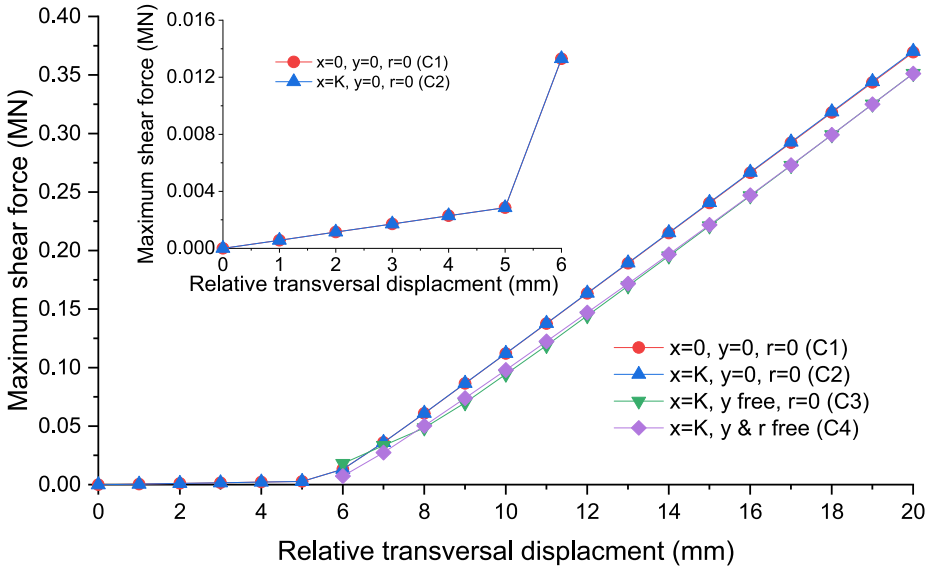

Fig. 22. The maximum shear force in the bolts, varying the relative transversal displacements between the adjacent segments of a circular joint, for different types of constraint on the endpoints of the bolt.

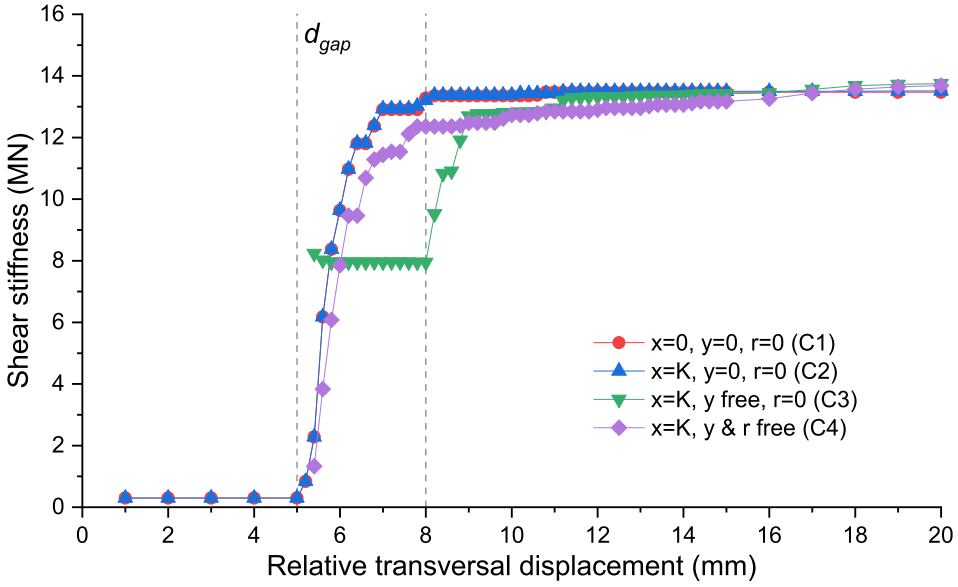

Fig. 23. The shear stiffness of the circular joint, varying the relative transversal displacements between the adjacent segments of a circular joint, for different types of constraint on the endpoints of the bolt.

The developed model is able to determine the shear stiffness of a segmental lining circular joint considering the interaction between the bolt and the concrete hole walls. The existing simplified equations of the shear stiffness due to the bolting system give higher values than those obtained by the proposed specific model due to the fact that they don't consider the interaction between the bolt and the hole wall during the second phase of the circular joint behaviour.

Since the curved bolts are widely used in tunnel segmental linings to connect lining rings along the circular joints, the shear deformation model of a curved bolt was also studied in this paper using the specific proposed numerical model. Although the structure of the bolt is symmetric with respect to the circular joint, the reaction forces in the hole and the deformation of the bolt are different on the two sides (inside the two adjacent segments), and for this reason the whole curved bolt is in this case analysed. A relative transversal displacement is applied on the right segment in order to analyse the stress and deformative condition of the bolt. Also in this case it was possible to analyse the contribution of the bolting system to the shear stiffness of the circular joint, noting how now the maximum value of the shear stiffness of the circular joint reached for a certain relative displacement of two adjacent segments is lower than that obtained in the case of a straight bolt.

The proposed model was then used to investigate the influence of two parameters that can be varied in the design stage of the tunnel segmental lining and also during its installation: the pretension force in the bolt and the gap between the hole wall and the bolt. It was verified that the pretension has a small influence on the shear force and can increase the maximum tensile stress developed in the bolt; instead, the increase of the gap leads to lower shear forces in the bolt, and extend the relative displacement value at which the maximum shear stiffness is reached. The results obtained by the proposed specific numerical model were compared with available laboratory test results, finding a good consistency between them and proving that the numerical model is

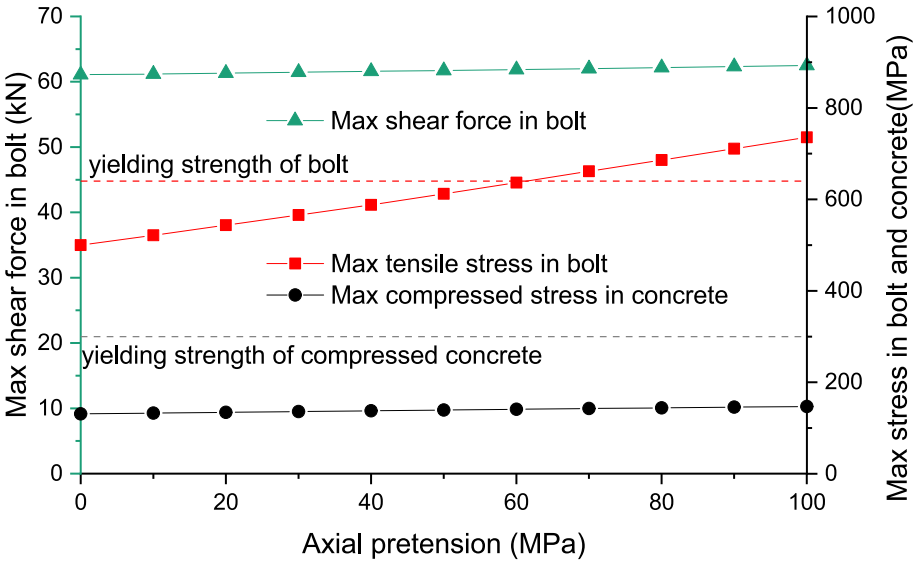

Fig. 24. The maximum shear force in the bolt, the maximum tensile stress in the bolt, and the maximum compressive stress in concrete on the hole wall, varying the axial pretension of the bolt at the endpoints (gap 5 mm).

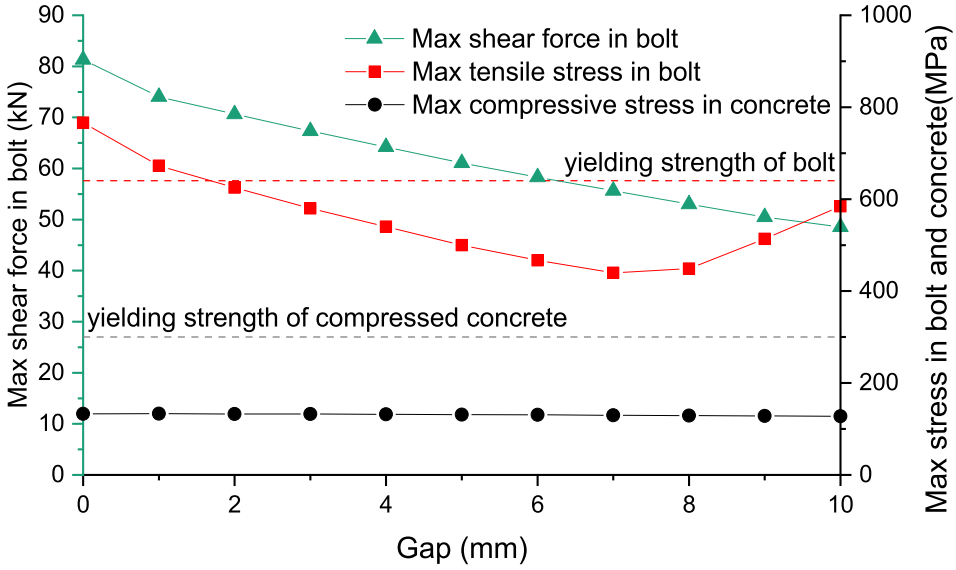

Fig. 25. The maximum shear force in the bolt, the maximum tensile stress in the bolt, and the maximum compressive stress in concrete on the hole wall, varying the gap (axial pretension of the bolt at the endpoints 0 MPa).

adequate in evaluating the bolt shear deformation and the shear behaviour of the circular joints connected by bolting systems in the case of both straight and curved bolts.

Finally, improving the compressive stiffness of the hole wall can effectively increase the shear stiffness of the circular joint, and the value of the joint shear stiffness can be evaluate based on the proposed model presented in this paper after a detailed test on the concrete foundation modulus of the hole wall.

Additionally, adopting the curved bolt and increasing the gap between the bolt and the hole wall will make the joint more softening; applying a greater pretension on the bolt the friction force on the joint will be increased with a weak impact on the shear force of the joint (the bolt axial force is perpendicular to the joint). Considering that the stronger joint stiffness will lead to a higher stress-state of the joint, which has a higher damage risk during the construction stage, the balance between the strength of the segmental lining concrete and the deformation performance of the lining needs to be evaluated using the proposed calculation method.

The proposed numerical model for the analysis of the behavior of the connection bolts of the precast concrete segments has proved to be a useful tool to be able to evaluate the mechanical behavior of circular joints and particularly to be able to determine the shear stiffness of this joint. This parameter is fundamental in order to obtain the stress and deformation state of the segmental lining and, therefore, to be able to carry out its correct sizing in the tunnel design phase.

CRediT authorship contribution statement

Xin Han: Methodology, Software, Validation, Formal analysis, Data curation, Writing – original draft, Visualization. **Pierpaolo Oreste:** Conceptualization, Methodology, Validation, Formal analysis, Writing – original draft, Writing – review & editing, Supervision. **Fei Ye:** Validation, Writing – review & editing, Supervision, Funding acquisition.

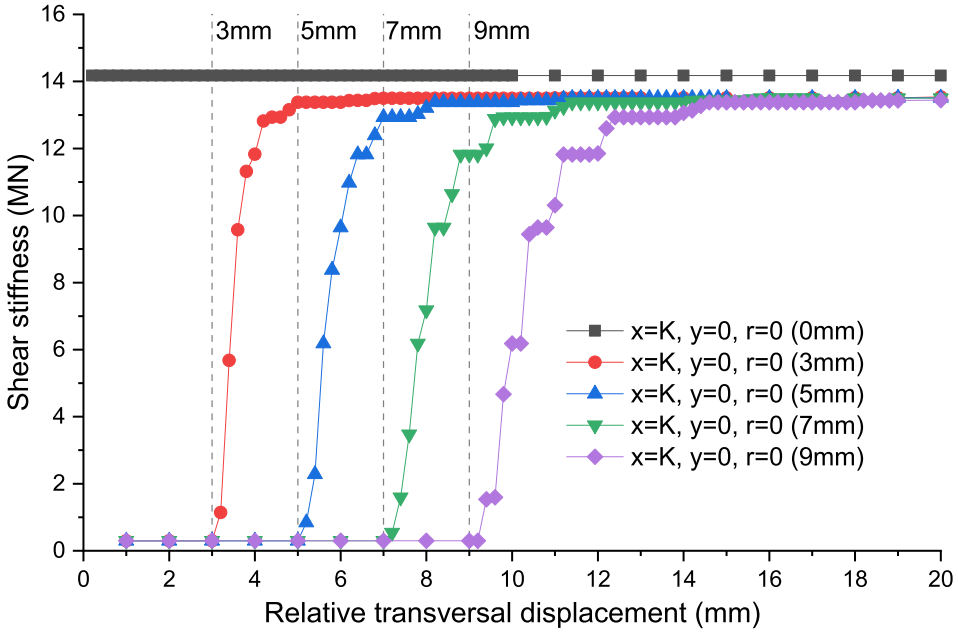

Fig. 26. The shear stiffnesses of the circular joint varying the relative transversal displacements between segments on the circular joint, for different gap values (type of constraint of case 2). The curves of the graph can be shared in three phases: an initial phase with a very low value of the shear stiffness; a second phase, with an increasing value, varying the relative transversal displacement; a third one, with a constant maximum value.

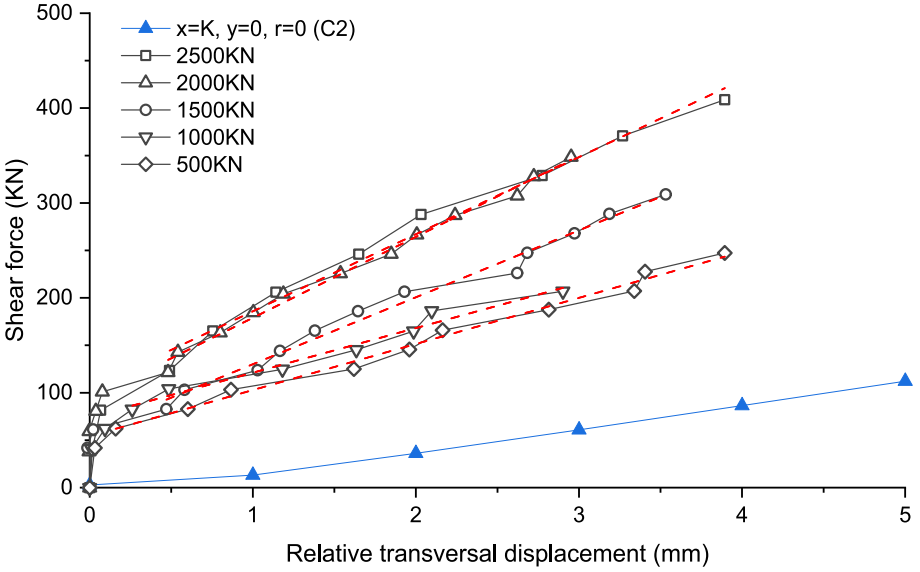

Fig. 27. The measured shear force values of the circular joint with different normal forces applied to the joint during laboratory tests (Zuo et al., 2022), compared with calculated results by the proposed numerical model (blue line). The dotted red lines refer to the measured average shear stiffness value during the laboratory tests.

Declaration of Competing Interest

The authors declare that they have no known competing financial interests or personal relationships that could have appeared to influence the work reported in this paper.

Data availability

No data was used for the research described in the article.

Acknowledgement

This study was financially supported by the Fundamental Research Funds for the Central Universities, CHD (Grant No. 300102212702) and the National Natural Science Foundation of China (No. 51878060), and this support are gratefully acknowledged. The first author also would like to appreciate the scholarship from China Scholarship Council (Grant No. 202106560030) for his study in Politecnico di Torino.

References:

Caggiano, A., Cremona, M., Faella, C., Lima, C., Martinelli, E., 2012. Fracture behavior of concrete beams reinforced with mixed long/short steel fibers. Constr. Build. Mater. 37, 832–840.

Chaipanna, P., Jongpradist, P., 2019. 3D response analysis of a shield tunnel segmental lining during construction and a parametric study using the ground-spring model. Tunn. Undergr. Space Technol. 90, 369–382.

Chen, R.-P., Meng, F.-Y., Ye, Y.-H., Liu, Y., 2018. Numerical simulation of the uplift behavior of shield tunnel during construction stage. Soils Found. 58 (2), 370–381.

Cheng, H., Chen, R., Wu, H., Meng, F., Yi, Y., 2021. General solutions for the longitudinal deformation of shield tunnels with multiple discontinuities in strata. Tunn. Undergr. Space Technol. 107, 103652.

China, 2021. Standard for design of shield tunnel engineering. China Architecture & Building Press. in Chinese.

Dastjerdy, B., Hasanpour, R., Chakeri, H., 2018. Cracking Problems in the Segments of Tabriz Metro Tunnel: A 3D Computational Study. Geotech. Geol. Eng. 36 (4), 1959–1974.

Do, N.A., Dias, D., Oreste, P., Djeran-Maigre, I., 2013. 2D numerical investigation of segmental tunnel lining behavior. Tunn. Undergr. Space Technol. 37, 115–127.

Do, N.A., Dias, D., Oreste, P., Djeran-Maigre, I., 2014. A new numerical approach to the hyperstatic reaction method for segmental tunnel linings. Int. J. Numer. Anal. Methods Geomech. 38 (15), 1617–1632.

Do, N.-A., Dias, D., Oreste, P., Djeran-Maigre, I., 2015. Behaviour of segmental tunnel linings under seismic loads studied with the hyperstatic reaction method. Soil Dyn. Earthquake Eng. 79, 108–117.

Do, N.-A., Dias, D., Oreste, P., 2016. 3D numerical investigation of mechanized twin tunnels in soft ground – Influence of lagging distance between two tunnel faces. Eng. Struct. 109, 117–125.

El-Ariss, B., 2007. Behavior of beams with dowel action. Eng. Struct. 29 (6), 899–903.

Feng, K., He, C., Qiu, Y., Zhang, L., Wang, W., Xie, H., Zhang, Y., Cao, S., 2018. Full-scale tests on bending behavior of segmental joints for large underwater shield tunnels. Tunn. Undergr. Space Technol. 75, 100–116.

Feng, H., Ye, F., Jiang, Y., Wang, J., Wen, X., Fang, Q., 2022. Effect of rolling angle on segment cracking and damage of shield tunnel - field investigation and modelling. Engineering Failure Analysis 140, 106584.

Geng, P., Mei, S.Y., Zhang, J., Chen, P.L., Zhang, Y.Y., Yan, Q.X., 2019. Study on seismic performance of shield tunnels under combined effect of axial force and bending moment in the longitudinal direction. Tunn. Undergr. Space Technol. 91, 13.

Gil Lorenzo, S., 2019. Longitudinal beam response of concrete segmental linings simultaneously backfilled with bicomponent grouts. Tunn. Undergr. Space Technol. 90, 277–292.

Han, X., Oreste, P., Ye, F., 2023a. The buoyancy of the tunnel segmental lining in the surrounding filling material and its effects on the concrete stress state. Geotech Geol Eng 41 (2), 741–758.

Han, X., Oreste, P., Ye, F., 2023b. The important role of stiffnesses values of circular joints on the stress state developed in the tunnel segmental lining. Geomech. Geophys. Geo-energ. Geo-resour. 9 (1).

He, X.G., Kwan, A.K.H., 2001. Modeling dowel action of reinforcement bars for finite element analysis of concrete structures. Computers and Structures 79 (6), 595–604.

Huang, H.W., Gong, W.P., Khoshnevisan, S., Juang, C.H., Zhang, D.M., Wang, L., 2015. Simplified procedure for finite element analysis of the longitudinal performance of shield tunnels considering spatial soil variability in longitudinal direction. Comput. Geotech. 64, 132–145.

Huang, L.C., Ma, J.J., Lei, M.F., Liu, L.H., Lin, Y.X., Zhang, Z.Y., 2020. Soil-water inrush induced shield tunnel lining damage and its stabilization: A case study. Tunn. Undergr. Space Technol. 97, 16.

Huang, W.M., Wang, J.C., Yang, Z.X., Xu, R.Q., 2022. Analytical analysis of the longitudinal response of shield tunnel lining considering ring-to-ring interaction. Computers and Geotechnics 146, 104705.

Khazaeeu, A., Ghalehnovi, M., 2018. Bearing Stiffness of UHPC; An Experimental Investigation and A Comparative Study of Regression and SVR-ABC Models. J. Adv. Concr. Technol. 16 (3), 145–158.

Koizumi, A., Murakami, H., Nishino, K., 1988. Study on the analytical model of shield tunnel in longitudianl direction. J. Jpn. Soc. Civ. Eng. 394, 79–88 in Japanese.

Li, Z.L., Soga, K., Wang, F., Wright, P., Tsuno, K., 2014. Behaviour of cast-iron tunnel segmental joint from the 3D FE analyses and development of a new bolt-spring model. Tunn. Undergr. Space Technol. 41, 176–192.

Li, X.J., Zhou, X.Z., Hong, B.C., Zhu, H.H., 2019. Experimental and analytical study on longitudinal bending behavior of shield tunnel subjected to longitudinal axial forces. Tunn. Undergr. Space Technol. 86, 128–137.

Liang, R., 2019. Simplified analytical method for evaluating the effects of overcrossing tunnelling on existing shield tunnels using the nonlinear Pasternak foundation model. Soils Found. 59 (6), 1711–1727.

Liang, R.Z., Xia, T.D., Huang, M.S., Lin, C.G., 2017. Simplified analytical method for evaluating the effects of adjacent excavation on shield tunnel considering the shearing effect. Comput. Geotech. 81, 167–187.

Liang, L., Xu, C., Zhu, B., Deng, J., 2020. Theoretical method for an elastic infinite beam resting on a deformable foundation with a local subsidence. Computers and Geotechnics 127, 103740.

Liao, S.-M., Peng, F.-L., Shen, S.-L., 2008. Analysis of shearing effect on tunnel induced by load transfer along longitudinal direction. Tunn. Undergr. Space Technol. 23 (4), 421–430.

Liu, X., Dong, Z.B., Song, W., Bai, Y., 2018. Investigation of the structural effect induced by stagger joints in segmental tunnel linings: Direct insight from mechanical behaviors of longitudinal and circumferential joints. Tunn. Undergr. Space Technol. 71, 271–291.

Liu, X., Feng, K., He, C., Zhao, L., 2022. Prototype test of the mechanical behavior and failure mechanism of segment structure with distributed mortises and tenons. Structural Concrete 23 (5), 2837–2851.

Liu, D.J., Wang, F., Hu, Q.F., Huang, H.W., Zuo, J.P., Tian, C., Zhang, D.M., 2020b. Structural responses and treatments of shield tunnel due to leakage: A case study. Tunn. Undergr. Space Technol. 103, 18.

Liu, D.J., Tian, C., Wang, F., Hu, Q.F., Zuo, J.P., 2021a. Longitudinal structural deformation mechanism of shield tunnel linings considering shearing dislocation of circumferential joints. Comput. Geotech. 139, 15.

Liu, B.o., Yu, Z., Han, Y., Wang, Z., Zhang, R., Wang, S., 2020a. Analytical solution for the response of an existing tunnel induced by above-crossing shield tunneling. Computers and Geotechnics 124, 103624.

Liu, X., Zhang, Y.M., Bao, Y.H., 2020c. Full-scale experimental investigation on stagger effect of segmental tunnel linings. Tunn. Undergr. Space Technol. 102, 14.

Ma, S., Zhao, Z., Peng, J., Gui, Y., 2018. Analytical modeling of shear behaviors of rockbolts perpendicular to joints. Constr. Build. Mater. 175, 286–295.

Ma, S., Zhao, Z., Shang, J., 2019. An analytical model for shear behaviour of bolted rock joints. Int. J. Rock Mech. Mining Sci. 121, 104019.

Maekawa, K., Qureshi, J., 1996. Computational Model for Reinforcing Bar Embedded in Concrete under Combined Axial Pullout and Transverse Displacement. J. Mater. Conc. Struct. 1996 (538), 227–239.

Moradi, A.R., Soltani, M., Tasnimi, A.A., 2012. A Simplified Constitutive Model for Dowel Action across RC Cracks. J. Adv. Concr. Technol. 10 (8), 264–277.

Oreste, P.P., 2007. A numerical approach to the hyperstatic reaction method for the dimensioning of tunnel supports. Tunn. Undergr. Space Technol. 22 (2), 185–205.

Oreste, P.P., 2009. Face stabilisation of shallow tunnels using fibreglass dowels. Proc. Inst. Civ. Eng. Geotech. Eng. 162 (2), 95–109.

Oreste, P.P., Cravero, M., 2008. An analysis of the action of dowels on the stabilization of rock blocks on underground excavation walls. Rock Mech. Rock Eng. 41 (6), 835–868.

Oreste, P., Spagnoli, G., Luna Ramos, C.A., Sebille, L., 2018. The Hyperstatic Reaction Method for the Analysis of the Sprayed Concrete Linings Behavior in Tunneling. Geotech. Geol. Eng. 36 (4), 2143–2169.

Oreste, P., Sebastiani, D., Spagnoli, G., de Lillis, A., 2021. Analysis of the behavior of the two-component grout around a tunnel segmental lining on the basis of experimental results and analytical approaches. Transportation Geotechnics 29, 100570.

Prates Aguiar, O., Barreto Caldas, R., 2022. Circular openings with transverse rebar as steel-concrete shear connection (part 1/2): Analytical model for strength and slip capacity. Eng. Fail. Anal. 133, 106007.

Ranjbarnia, M., Fahimifar, A., Oreste, P., 2014. A simplified model to study the behavior of pre-tensioned fully grouted bolts around tunnels and to analyze the more important influencing parameters. J. Mining Sci. 50 (3), 533–548.

Shi, C.H., Wang, Z.X., Gong, C.J., Liu, J.W., Peng, Z., Cao, C.Y., 2022. Prediction of the additional structural response of segmental tunnel linings induced by asymmetric jack thrusts. Tunn. Undergr. Space Technol. 124, 19.

Shiba, Y., Kawashima, K., Obinata, N., Kano, T., 1988. An evaluation method of longitudinal stiffness of shield tunnel linings for application to seismic response analyses. J. Jpn. Soc. Civ. Eng 1988 (398), 319–327.

Sørensen, J.H., Hoang, L.C., Olesen, J.F., Fischer, G., 2017. Testing and modeling dowel and catenary action in rebars crossing shear joints in RC. Eng. Struct. 145, 234–245.

Soroushian, P., Obaseki, K., Rojas, M.C., Sim, J., 1986. Analysis of Dowel Bars Acting Against Concrete Core. ACI Journal 642–649.

Soroushian, P., Obaseki, K., Rojas, M.C., 1987. Bearing strength and stiffness of concrete under reinforcing bars. ACI Mater. J. 84, 179–184.

Talmon, A.M., Bezuijen, A., 2013. Analytical model for the beam action of a tunnel lining during construction. Int. J. Numer. Anal. Methods Geomech. 37 (2), 181–200.

Vintzēleou, E.N., Tassios, T.P., 1986. Mathematical models for dowel action under monotonic and cyclic conditions. Mag. Concr. Res. 38 (134), 13–22.

Wang, H., 2020. Research on design scheme of shield tunnel crossing the Yangtze River for China-Russia eastern gas pipeline. China University of Geosciences (Beijing), Beijing. in Chinese.

Wang, F., Huang, H., Soga, K., Li, Z., 2021. 3D modelling of concrete tunnel segmental joints and the development of a new bolt-spring model. Tunn. Undergr. Space Technol. 110, 103835.

Wang, Z.X., Shi, C.H., Gong, C.J., Lei, M.F., Liu, J.W., Cao, C.Y., 2022. An enhanced analytical model for predicting the nonlinear longitudinal equivalent bending stiffness of shield tunnels incorporating combined N-M actions. Tunn. Undergr. Space Technol. 126, 18.

Wu, H.N., Shen, S.L., Liao, S.M., Yin, Z.Y., 2015. Longitudinal structural modelling of shield tunnels considering shearing dislocation between segmental rings. Tunn. Undergr. Space Technol. 50, 317–323.

Wu, H.N., Shen, S.L., Yang, J., Zhou, A.N., 2018. Soil-tunnel interaction modelling for shield tunnels considering shearing dislocation in longitudinal joints. Tunn. Undergr. Space Technol. 78, 168–177.

Matsunaga, K., Takase, Y., Abe, T., 2021. Modeling of dowel action for cast-in and post-installed anchors considering bond property. Eng. Struct. 245. https://www.sciencedirect.com/science/article/pii/S0141029621009238.

Xu, P., 2021. Study on shear performance of ring joint with distributed tenon for shield tunnel. Southwest Jiaotong University, Chengdu. in Chinese.

Yu, H.T., Cai, C., Bobet, A., Zhao, X., Yuan, Y., 2019. Analytical solution for longitudinal bending stiffness of shield tunnels. Tunn. Undergr. Space Technol. 83, 27–34.
Yu, J., Li, H., Huang, M., Li, Y., Tan, J.Q.W., Guo, Y., 2022. Timoshenko-beam-based response of existing tunnel to single tunneling underneath and numerical verification of opening and dislocation. Computers and Geotechnics 147, 104757.
Zaheri, M., Ranjbarnia, M., Dias, D., Oreste, P., 2020. Performance of segmental and shotcrete linings in shallow tunnels crossing a transverse strike-slip faulting. Transportation Geotechnics 23, 100333.
Zhang, W., Zhang, Q., Zhang, G., Song, C., 2020. Analysis on Shear Performance of 1.2m Segment Ring Tenon Joint in Tianjin Metro. Chinese J. Underground Space Eng. 16, 9 in Chinese.
Zhao, S., Zhang, D., Huang, Z., 2022. Mechanical Characteristics of Distributed Mortise-and-Tenon of Large-diameter Shield tunnels. Mod. Tunn. Technol. 59, 9 in Chinese.
Zhou, S., Ji, C., 2014. Tunnel segment uplift model of earth pressure balance shield in soft soils during subway tunnel construction. Int. J. Rail Transp. 2 (4), 221–238.
Zuo, L., Zhang, J., Feng, K., Yang, W., Zhang, L.i., He, C., 2022. Experimental study on Inter-ring joint shearing characteristics of gas transmission shield tunnel with bent bolt and tenon. Tunn. Undergr. Space Technol. 130, 104732.